HHS Public Access

Author manuscript

Cell Syst. Author manuscript; available in PMC 2019 December 26.

Published in final edited form as:

Cell Syst. 2018 December 26; 7(6): 627–642.e6. doi:10.1016/j.cels.2018.10.010.

Interactome and proteome dynamics uncover immune modulatory associations of the pathogen sensing factor cGAS

Krystal K. Lum, **Bokai Song**, **Joel D. Federspiel**, **Benjamin A. Diner**, **Timothy Howard**, and **Ileana M. Cristea***

Department of Molecular Biology, Princeton University, Princeton, NJ 08544

Summary

Viral DNA sensing is an essential component of mammalian innate immune response. Upon binding viral DNA, the cyclic-GMP-AMP synthase (cGAS) catalyzes the production of cyclic dinucleotides to induce type I interferons. However, little is known about how cGAS is homeostatically maintained or regulated upon infection. Here, we define cytoplasmic cGAS interactions with cellular and viral proteins upon herpes simplex virus (HSV-1) infection in primary human fibroblasts. We compare several HSV-1 strains (wild-type, *d109*, *d106*) that induce cytokine responses and apoptosis, and place cGAS interactions in the context of temporal proteome alterations using isobaric-labeling mass spectrometry. Follow-up analyses establish a functional interaction between cGAS and 2'−5'-oligoadenylate synthase-like protein OASL. The OAS-like domain interacts with the cGAS Mab21 domain, while the OASL ubiquitin-like domain further inhibits cGAS-mediated interferon response. Our findings explain how cGAS may be inactively maintained in cellular homeostasis, with OASL functioning as a negative feedback loop for cytokine induction.

eTOC

Lum, *et al.* characterize the global protein interactome of the DNA sensor, cGAS, in cellular homeostasis and during HSV-1 infection. Integrating quantitative proteomics, CRISPR-Cas9 technology, reciprocal isolations, and cytokine assays, the function of the discovered cGASOASL interaction suggests negative interferon regulation and crosstalk between the DNA and RNA sensing pathways.

Graphical Abstract

* Corresponding Author and Lead Contact: Ileana M. Cristea, Department of Molecular Biology, Princeton University, Princeton, NJ 08544, icristea@princeton.edu.

Author Contributions

Conceptualization, K.K.L., J.D.F., B.A.D., and I.M.C; Methodology, K.K.L., J.D.F., B.A.D., and I.M.C.; Investigation, K.K.L., B.S., J.D.F., B.A.D. and T.H.; Writing- Original Draft, K.K.L., B.S. and I.M.C.; Writing- Review & Editing, K.K.L., J.D.F., and I.M.C., Visualization, K.K.L., B.S., J.D.F., and I.M.C., Supervision, I.M.C.

Declaration of Interests

The authors declare no competing interests.

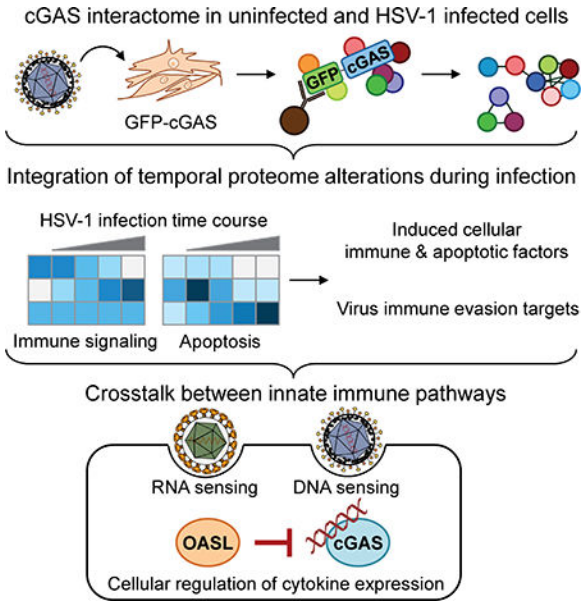

Introduction

Central to mammalian intrinsic and innate immunity is the ability of cells to recognize pathogenic moieties and induce the expression of interferon (IFN) and pro-inflammatory cytokines. It has long been understood that, in response to infection with DNA viruses, cells can distinguish viral DNA from genomically-stable host DNA to elicit such immune responses. To accomplish this, cells employ constitutively expressed DNA sensors that survey the intracellular space for pathogenic DNA. Among these, the discovery of the cyclic-GMP-AMP synthase (cGAS) (formerly C6ORF150 and MB21D1) as a prominent DNA sensor has brought critical insights into the mechanisms underlying the recognition of pathogenic DNA for immune response (Sun et al., 2013, Wu et al., 2013).

Upon sensing and binding to viral DNA, cGAS catalyzes the production of the cyclic dinucleotide 2’3’-cyclic GMP-AMP (cGAMP) from ATP and GTP (Fig. 1A). This second messenger activates a central cytoplasmic axis, comprised of the endoplasmic reticulum (ER)-associated adaptor STING, kinase TBK1, and transcription factor IRF3. Specifically, cGAMP binding to STING facilitates homo-dimerization of STING, followed by TBK1 recruitment and IRF3 phosphorylation, dimerization, and nuclear translocation (Fig. 1A). Nuclear IRF3 activates the transcription of antiviral IFNs and cytokines, which induce the expression of immunomodulatory interferon stimulated genes (ISGs). Hundreds of ISGs have been identified and shown to regulate diverse immunomodulatory pathways, prime cells for pathogen detection, arrest the cell cycle, or inhibit stages of pathogen replication and spread IRF3 activation has also been linked to virus-induced apoptosis (Chattopadhyay et al., 2010). Indeed, we found that cGAS-mediated immune response can activate caspase-3 and apoptosis in a STING-dependent manner (Diner et al., 2016).

The importance of cGAS in DNA sensing and immunity was highlighted under diverse contexts. Even outside the context of infection, the presence of transfected or damaged DNA

in the cytoplasm was shown to activate the cGAS-STING pathway (Li et al., 2013c, Diner et al., 2013). Furthermore, cGAS was demonstrated to act in defense against numerous viruses, including cytoplasmic- and nuclear-replicating DNA viruses, such as herpes simplex virus type 1 (HSV-1) and several RNA viruses, in particular human immunodeficiency virus (Gao et al., 2013, Li et al., 2013b, Wu et al., 2013, Paijo et al., 2016, Aguirre et al., 2017).

Despite this well-established function of cGAS in sensing foreign DNA, it is not fully understood how cGAS activity is regulated. For example, it remains unclear how cGAS is homeostatically maintained in an inactive state. This is important for understanding how cells return to a resting state after immune activation and how aberrant immune signaling can be linked to critical autoimmune diseases. Another unanswered question is what signals target cGAS to cytoplasmic DNA. It is possible that regulating cGAS activity relies in part on protein interactions. Thus far, studies in various cell types and under diverse experimental conditions have reported only few validated cGAS interactions with cellular proteins. Some of these demonstrated immune-enhancing effects, such as its associations with IFI16 (Orzalli et al., 2015), PQBP1 (Yoh et al., 2015), TRIM14 (Chen et al., 2016), XRCC6, HEXIM1 (Morchikh et al., 2017), TRIM56 (Seo et al., 2018), and ZCCHC3 (Lian et al., 2018). The negative regulation of cGAS has been explored under specific biological conditions, and shown to involve associations with BECN1 (Liang et al., 2014), AKT1 (Seo et al., 2015), CCP5 and CCP6 (Xia et al., 2016), caspase-1 (Wang et al., 2017), NCOA3 (Wu et al., 2017), and NONO (Lahaye et al., 2018). Viruses were also reported to suppress IFN response by using viral proteins to target cGAS, such as ORF52 and LANA from Kaposi's sarcoma-associated herpesvirus (KSHV) (Wu et al., 2015, Zhang et al., 2016), NS2B from Dengue virus (Aguirre et al., 2017), and UL37 from HSV-1 (Zhang et al., 2018). The above interactions were predominantly found via analyses focused on certain proteins or pathways, or via testing hypothesized binary interactions. Hence, a global assessment of cGAS interactions in normal cells or during active immune signaling remained to be performed.

Here, we characterized cytoplasmic cGAS protein interactions in cellular homeostasis and upon HSV-1 infection in primary human fibroblasts. We placed cGAS interactions in the context of infection-driven proteome alterations and compared temporal changes upon infections with several HSV-1 strains (wild type (WT), *d106*, and *d109*) that induce varying levels of cytokines or apoptosis. These comparisons provide an in-depth knowledge of the cellular proteomic landscape during HSV-1 infection and identify cGAS interactions with both cellular and viral proteins. Integration of quantitative mass spectrometry (MS), reciprocal isolations, domain constructions, and cytokine assays allowed us to establish a functional interaction between cGAS and another immune response factor, OASL. We show that OASL suppresses cGAS-mediated IFN response, suggesting that it functions as a regulatory negative feedback loop for cytokine induction. Altogether, our findings provide an explanation for how cGAS may be maintained inactively in cells, contributing insights into mechanisms that balance healthy levels of IFN signatures.

Results and Discussion

A cell-based system to identify cGAS protein interactions during immune signaling upon HSV-1 infection.

The study of cGAS at the endogenous level has been hampered by the limited availability of antibodies for either immunoblotting, immunofluorescence, or immunoaffinity purification (IP). Despite testing numerous commercially available antibodies, our initial attempts to isolate endogenous cGAS were unsuccessful. This is likely driven by the low affinity and specificity of these antibodies, but also by the relatively low abundance of endogenous cGAS in several tested cell types, including fibroblasts (Wu et al., 2013). Therefore, to understand cGAS regulation in cells, we first needed to design a system that would allow us to define cGAS protein interactions. We constructed plasmids that harbor human cGAS tagged with green fluorescent protein (GFP) (Fig. S1A). Co-transfection of STING with either N- or C-terminally tagged cGAS in HEK293Ts demonstrated activation of the immune signaling marker phosphorylated TBK1 (Fig. 1B). Both tagged versions of cGAS expressed well and at comparable levels. To avoid possible interference with other functions (i.e., IFN-independent) of the conserved C-terminal nucleotidyltransferase (NTase) and Male Abnormal 21 (Mab21) domains, we chose to focus on the N-terminally tagged cGAS construct (GFP-cGAS). Further validating the activity of this construct, HEK293Ts expressing GFP-cGAS and STING were capable of inducing cytokine (*ifn-β, isg54, and isg56*) expression to a similar extent as non-tagged cGAS- and STING- expressing cells (Fig. 1C).

To gain insights into how cGAS activity is controlled in resting cells and in response to HSV-1 infection, we used IP of GFP-cGAS coupled to quantitative MS to define its interactions in both uninfected and infected cells (Figs. 1D and S1B). We selected primary human fibroblasts (HFFs) owing to the abundance of studies demonstrating cGAS-dependent antiviral activity during HSV-1 infection (Li et al., 2013c, Wu et al., 2013, Li et al., 2013b, Zhang et al., 2014) and the presence of active immune signal pathway components in this cell type. Similar to the HEK293Ts, we first confirmed the inducible expression of GFP-cGAS in HFFs (Fig. S1C). Next, we either mock-infected (uninfected) or infected HFFs with WT HSV-1. Cells were harvested at 6 hours post-infection (hpi), when cytokine levels were reported to be elevated during HSV-1 infection (Orzalli et al., 2012). Infected cells expressing GFP-cGAS were capable of inducing cytokine expression to a higher extent than uninfected cells or GFP-expressing control cells (Fig. S1D).

Given the known predominant cytoplasmic DNA sensing function of cGAS, we performed cellular fractionation to focus on cytoplasmic cGAS protein interactions and reduce possible non-specific background from other cellular compartments. Experiments were performed in biological duplicates, and the efficiencies of the cytoplasmic fractionation (Fig. 1E) and GFP-cGAS isolation (Fig. 1F) were confirmed. Co-isolated proteins were analyzed by nLC-MS/MS on a Q Exactive HF mass spectrometer. Non-specific interactions were filtered first by using the ‘significance analysis of interactome’ (SAINT) probabilistic scoring (Choi et al., 2011), and then by comparison with the CRAPome database (Mellacheruvu et al., 2013) (Fig. S1E). The majority of our SAINT-filtered cGAS interactions were found in less than

20% of the 552 control IPs deposited in CRAPome (Table S1), supporting the stringency of our isolation conditions. Comparison of the biological replicates during mock and WT HSV-1 infections demonstrated the reproducibility of the isolations, as candidate interactions had similar spectral abundances upon bait normalization (Fig. S1F).

cGAS interacts with interferon-induced proteins, including OAS family proteins.

Our analysis identified cGAS associations with both cellular and viral proteins, the majority of which have not been previously reported (Table S2). Of the few known interactions in other cells types, in HFFs we similarly identified cGAS associations with the IFN-induced TRIM14 and IFI16, the type III IFN-inducing cytosolic DNA sensor XRCC6, the immune-modulatory co-DNA sensor ZCCHC3, as well as the HSV-1 protein UL37. XRCC6 was removed from the final interaction network due to having 51% presence in the CRAPome repository (Table S1). The relative enrichments of cGAS interactions were assessed by calculating normalized spectral abundance factors for each protein (Fig. S2). Assembly of an interaction network categorized by gene ontology highlighted the association of cGAS with cellular proteins involved in mitochondria maintenance, immune signaling, apoptosis, endomembrane transport, signal transduction, and virus replication (Fig. 2).

Among the cellular proteins implicated in immune signal processing and amplification were other DNA sensors (DDX60, DHX36, and IFI16), interferon-induced proteins with tetratricopeptide repeats (IFIT1, IFIT2, IFIT3, IFITM3), tripartite motif proteins, and cytosine deaminases. We additionally identified cGAS associations with oligoadenylate synthase family proteins OASL and OAS2, with OASL being the most enriched interaction relative to all other immune proteins (Fig. S1F). This is perhaps surprising, as OAS proteins are well-known for functioning in sensing viral dsRNA, rather than dsDNA (Hornung et al., 2014). Remarkable structural and functional parallels have been shown between cGAS and OAS proteins. These proteins have similar structural folds that undergo conformational switches for their enzymatic activities upon binding to double-stranded nucleic acids. Specifically, cGAS, OAS1, OAS2, and OAS3 are sequence-independent NTases that generate exclusive classes of 2’−5’-linked second messengers. Notably, OASL, the most prominent cGAS-OAS protein interaction, contains an N-terminal OAS-like domain, yet lacks 2’−5’ oligoadenylate synthase activity due to active site differences (Rebouillat et al., 1998). OASL was reported to have both anti- and pro-viral activities in different biological systems, as human OASL was shown to activate the RNA sensor RIG-I (Zhu et al., 2014) and mouse *Oasl1* inhibited type I IFN production by suppressing the translation of IRF7 (Lee et al., 2013). It is tempting to speculate that these associations may represent concerted strategies employed by cells to maintain the fine-balance between homeostasis and immune signaling.

Consistent with its role in inducing apoptosis through STING, we also identified enriched cGAS associations with cellular proteins involved in ubiquitination and DNA damage response (USP10, DTX3L, UFL1, and UEVLD). cGAS also associated with mitochondrial proteins, including ribosomal subunit proteins, in agreement with its reported peri-mitochondrial localization for sensing leaked mitochondrial DNA during stress and viral infection, such as with HSV-1 (West et al., 2015).

Our study also identified previously unknown cGAS associations with HSV-1 proteins. Among these, the tegument protein VP16, encoded by UL48, has been shown to suppress IFN-β expression by inhibiting STING-activated transcription factors (Xing et al., 2013). Therefore, this cGAS association may represent an additional point of IFN antagonism upstream of STING. The cGAS-virus protein interaction found as most spectrally abundant was that with ICP6, encoded by UL39. ICP6 is a ribonucleotide reductase with roles in suppressing caspase-dependent apoptosis (Langelier et al., 2002). As cGAS was shown to be able to promote apoptosis (Diner et al., 2016), this association may serve as an accessory mechanism of virus suppression of apoptosis.

Altogether, these cGAS interactions with cellular and viral proteins can represent diverse mechanisms at the interface between cellular induction or viral suppression of innate immune response and apoptosis. However, whenever exploring such interactions, the temporal changes in protein abundances during the progression of infection must also be considered. This is particularly relevant for immune signaling proteins, as numerous cGAS interactions that we identified are known to be induced by interferon. Therefore, we proceeded to place this knowledge of cGAS associations in the context of their proteome abundance changes during HSV-1 replication.

Proteome alterations reflect the immune-evasion ability of WT HSV-1 and the immune- and apoptosis-stimulatory properties of *d106* HSV-1.

To explore cellular proteome abundance changes, we infected HFFs (MOI of 5, matching our interaction conditions) and harvested cells at 0 (mock), 2, 6, 12, and 18 hpi after infection with WT HSV-1 (Fig. 3A). Given the functions of cGAS in inducing immune response and apoptosis, as a positive control we additionally assessed temporal proteome changes during *d106* HSV-1 infection. This strain contains multiple immediate-early (IE) gene mutations (ICP4-, ICP22-, ICP27-, ICP47-) that render protein level deficiencies in both expression and activity (Fig. S1B), and is also known to more strongly induce cytokines and apoptosis than WT HSV-1 (Sanfilippo and Blaho, 2006, Diner et al., 2015). Comparison of the proteomes between these two viral strains can help point to proteins that regulate infection-induced cytokine expression and apoptosis.

We labeled all samples with isobaric tandem mass tags (TMT), which allowed for multiplexing and simultaneous relative quantification of detected proteins. Altogether, we identified 6,208 and 6,185 proteins during WT and *d106* HSV-1 infections, respectively, making this the most in-depth resource of viral and cellular proteins during HSV-1 infection (Fig. 3B and Tables S3–4). While the proteome of *d106* infection was not previously investigated, reassuringly our study was consistent with a report for WT HSV-1 infection (Kulej et al., 2017). Our identifications covered 93% of the previous proteome in fibroblasts, while also containing an additional 1,909 high-confidence identifications. Principal components analysis demonstrated that the biological replicates were similar to one another at each time point (Figs. 3C and S3A). Validating the known effects of WT HSV-1 infection, we observed declines in the levels of proteins targeted for degradation by the viral E3 ubiquitin ligase ICP0, including the antiviral ISG proteins IFI16, PML, and Sp100 (Fig. 3D,

left). An additional set of proteins similarly declined in abundance (Fig. 3D, right), and some of these may represent yet unclassified HSV-1 degradation targets.

Our results also provided the quantitative monitoring of sixty viral proteins during WT HSV-1 infection. Viral proteins constituted the top 1% of proteins most greatly upregulated across all infection time points (Fig. 3E). As expected, infection with *d106*, which lacks functional expression of the α genes, ICP4, ICP22, ICP27, and ICP47, significantly hampered the capacity of the virus to express 62% of the viral proteins at a detectable level (Tables S3–S4). Of the viral proteins detected during *d106* infection, a majority had significantly reduced abundances compared to those during WT HSV-1 infection across all temporally-coordinated gene classes (α, β, and γ). Two exceptions to this were the IE protein ICP0 and the early protein ICP6. Increased ICP0 expression during *d106*, relative to WT HSV-1 infection, may indicate a compensatory response induced by the virus to express the other IE genes and later gene classes. ICP6 was also expressed at levels comparable to WT HSV-1, indicating that expression of ICP0, possibly in coordination with ICP22, ICP4, or ICP47, was sufficient to aid ICP6 expression. While ICP6 levels were unaffected by *d106* mutations, US3 levels were below the limit of detection during *d106* infection. Given the known role of US3 in preventing Fas-mediated apoptosis (Jerome et al., 1999), the ability of cells to promote cell death upon *d106* infection may be connected to the absence of US3 or the presence of cellular factors, upregulated during *d106* infection relative to WT HSV-1, that can counteract ICP6. In line with this, we further identified a subset of upregulated proteins during *d106* infection with known roles in inducing apoptosis, including BCL6, FAS, DDX20, and IFIT2 (Fig. 3F).

To investigate the levels of cellular proteins that may contribute to cGAS functions, we further focused on proteins that upregulate immune response. Protein levels of cGAS itself were moderately increased (1.1-fold) throughout WT HSV-1 infection and were elevated by ~2-fold during *d106* infection, in agreement with the higher immune-activating capacity of this virus strain (Fig. 3G). The innate immune signaling protein IFI16 had decreased abundance levels in both virus infections. This was expected given that both viruses have ICP0, a viral E3 ubiquitin ligase that targets IFI16 for degradation. In contrast, many innate immune proteins were significantly higher in cells infected with *d106* when compared to WT at 18 hpi (Fig. S3B). These included the interferon inducible proteins (IFIT1–3, MX1), the RNA sensor RIG-I and one of its partner proteins, OASL, the transcription factor ATF3, the cell proliferation protein GAS6, as well as proteins of unknown function (NMES1, ERICH1) (Fig. S3C). A nearly 4-fold upregulation was evident for OASL during *d106* infection, in contrast to its relatively unchanged levels during WT HSV-1 when compared to mock cells. Altogether, our temporal proteome analysis during immune-modulating HSV-1 infections revealed dynamic changes in proteins that regulate immune signaling and apoptosis.

Validation of the temporal regulation of cGAS and OAS protein abundances during infection with different HSV-1 strains.

Considering the OASL upregulation during active immune signaling upon *d106* infection, and it being the most enriched cellular association of cGAS, we gained interest in further

exploring the cGAS interactions with OAS proteins. We first aimed to more accurately monitor the abundances of cGAS, OASL, and OAS2 during the HSV-1 life cycle. Additionally, our TMT study did not identify detectable OAS2 levels. Therefore, we designed a quantitative targeted MS approach based on parallel-reaction monitoring (PRM) to specifically quantify the abundance levels of these proteins (Fig. 4A). The detection of signature peptides for each protein allowed us to quantify their levels at different time points of the HSV-1 replication cycle. ICP6 and ICP0 peptides were additionally included as infection markers. TUBA1A and MYH9 peptides were monitored in parallel as controls for proteins that did not undergo infection-induced changes. During WT HSV-1 infection, cGAS, OASL, and OAS2 did not increase in abundance by 6 hpi (Fig. 4B and Table S5). This is consistent with the reported low levels of cytokines induced during WT infection (Mogensen et al., 2004, Diner et al., 2015), as well as the absence of upregulated ISGs (Fig. 3G) and our whole proteome results. To confirm the capacities of these three proteins to be upregulated during active immune signaling, we further monitored their levels during infection with either *d106* or *d109* HSV-1. The *d109* strain lacks expression of all IE gene products (Fig. S1B), rendering it both replication-incompetent and incapable of expressing viral gene products (Samaniego et al., 1998). Previous reports demonstrated that *d109* induced strong levels of cytokines in HFFs at levels higher than both WT and *d106* HSV-1 (Orzalli et al., 2012, Orzalli et al., 2015). Yet, in contrast to *d106*, *d109* is not known to induce apoptosis, and comparisons among these infections can support whether these proteins are induced specifically as a result of immune signaling. Infection with either *d106* or *d109* displayed little to no upregulation of cGAS, OASL, and OAS2 at 6 hpi. However, the levels of OASL and OAS2 were strongly increased by 18 hpi during both *d106* and *d109* infections, by ~8-fold and 2-fold for OAS2 and ~25-fold and 3-fold for OASL, respectively.

cGAS interactions in the context of proteome alterations during immune signaling.

Having measured the temporal proteomes of fibroblasts infected with these different HSV-1 strains, we next assessed whether the abundances of the proteins that we identified as cGAS interactions (Fig. 5, left) contribute to their enriched associations with cGAS at 6 hpi (Fig. 5, WT IP/TMT). We observed up to a 3-log enrichment of ISG proteins interacting with cGAS relative to their endogenous levels at 6 hpi. The little to no increase in ISG protein levels (e.g., OASL, OAS2, IFIT1/2/M3, MX1/2, TRIM14, TRIM25, and APOBEC3C/D/F/G) relative to their enrichment in the IPs substantiates the specificity and enrichment of their interactions with cGAS during our mock and WT HSV-1 infection conditions. Our finding that a majority of cGAS interactions were identified during both mock and WT HSV-1 infection prompted us to assess if these interactions were also maintained during active immune signaling. To test this, we performed an additional IP-MS study (in biological duplicate) of cGAS interactions in HFFs upon infection with *d109* HSV-1 (Fig. 1D and Fig. 5, right), the strain that induces higher cytokine levels than WT or *d106* (Fig. S1B) (Orzalli et al., 2012). Except for USP7 and PRKRA (Fig. 5, middle, asterisks), all cGAS interactions with immune proteins were retained upon *d109* infection. The maintenance of these associations across mock, WT HSV-1, and *d109* infections suggests that some of these likely represent cGAS interactions during cellular homeostasis.

The cGAS-OASL interaction is maintained across cell types in uninfected and infected cells upon DNA stimulation.

In all cGAS isolations from mock, WT or *d109* infected cells, OASL was consistently identified as one of the most spectrally enriched cGAS interactions (Fig. 2, S1F, and S2). We asked whether this specific interaction would be affected not only by a state of increased immune signaling relative to WT HSV-1 infection, but also by the presence of cytoplasmic DNA and by cell type. First, in HFFs during *d106* infection, we observed a consistent and specific association of OASL with cGAS when comparing GFP-cGAS to GFP control isolations (Fig. 6A). We then proceeded to transfect cells with DNA to mimic conditions in which high levels of DNA are present to activate cytoplasmic cGAS. For this, we implemented a system used extensively in previous reports characterizing cGAS DNA sensing (Diner et al., 2013, Gao et al., 2013, Zhang et al., 2014). Specifically, we used HEK293Ts, given the undetectable levels of endogenous cGAS and STING in these cells and, therefore, the ability to minimally reconstitute this immune signaling pathway by stably expressing STING (293T-STING) and inducibly expressing GFP-cGAS. We confirmed cytokine expression in these cells upon cGAS expression (Fig. S4). Next, we transfected cells with a 70-base pair DNA sequence from the vaccinia virus genome (VACV 70mer), as DNA sensors were reported to bind to this substrate (Li et al., 2012). Upon IP-MS of GFP-cGAS in 293T-STINGs during mock and VACV 70mer DNA transfection, we found cGAS to consistently and specifically associate with OASL (Fig. 6B).

As these identifications were conducted using an overexpression system, we further sought to confirm this cGAS-OASL association endogenously by IP-MS. As stated above, given our unsuccessful attempts to isolate endogenous cGAS from HFFs, we used PRM to find a relevant immune cell type that has higher levels of cGAS, and compared endogenous cGAS levels in HFFs and differentiated THP-1 monocytes. We identified a 21-fold higher abundance of cGAS in THP-1s relative to HFFs (Fig. 6C), which encouraged us to assess the endogenous cGAS-OASL association in THP-1s. Following IP-MS of endogenous cGAS in mock and HSV-1-infected differentiated THP-1s, we observed an enriched co-isolation of OASL with cGAS relative to IgG control isolations (Fig. 6D). The OASL-cGAS association was more prominent upon WT HSV-1 infection than in uninfected cells, similar to our observation in HFFs.

To further expand our validations of cGAS protein interactions that we identified, we conducted a series of reciprocal isolations using antibodies against the endogenous proteins in WT HSV-1-infected GFP and GFP-cGAS HFFs. We selected OAS2 given its structural similarities to cGAS, ASCC3 for its known immune-regulatory role in dampening ISG expression during West Nile Virus infection (Li et al., 2013a), and the viral protein ICP0 for its high spectral enrichment with cGAS (Table S2). Using PRM, we quantified peptides unique to each protein. We confirmed both isolation of the bait proteins in GFP and GFP-cGAS HFFs, as well as their enriched associations with cGAS specifically in GFP-cGAS cells when compared to GFP cells (Fig. 6E and Table S6). Upon ectopic expression of GFP-cGAS and ICP0, we conducted an additional IP of ICP0 and observed successful co-isolation of cGAS (Figure 6F). Altogether, these experiments provide confidence in the identified network of cGAS interactions with cellular and viral proteins. They further

highlight a prominent interaction with OASL in multiple cell types, as well as under both mock-treated and DNA-stimulatory conditions.

OASL associates via the oligoadenylate synthase-like domain and negatively regulates cGAS-mediated interferon response.

The preserved nature of the cGAS-OASL interaction in uninfected, HSV-1-infected, and DNA-transfected cells within multiple cell types prompted us to explore the functional significance of this association. We first assessed which OASL domain mediates its interaction with cGAS. To accomplish this, we tested the interaction of cGAS with the two known isoforms of OASL, p30 and p59 (Fig. 7A). Both isoforms contain an OAS-like domain, yet are differentiated by the presence of two tandem ubiquitin-like (UBL) domains at the C-terminus of p59. The UBL domains are known to activate RIG-I during sensing of viral RNA genomes (Zhu et al., 2014). Upon co-expression of GFP-cGAS and Flag-OASL p59 in cells, we observed cytoplasmic co-localization in both uninfected and HSV-1-infected cells (Fig. 7B). Using Flag-tagged p30 and p59 constructs, we next determined that cGAS interacted with both OASL isoforms (Fig. 7C). This suggested that the interaction can be facilitated via the OAS-like domain and does not require the UBL domains. We further determined that the Mab21 domain of cGAS maintained an enriched association with both OASL isoforms, relative to full-length cGAS (Fig. 7D). These experiments further substantiate the cGAS-OASL interaction, and suggest that the OASL oligoadenylate synthase-like domain can associate with the cGAS Mab21 domain.

To explore the functional relationship between cGAS and OASL, we tested the capacity of the interacting proteins to affect cytokine induction when co-expressed. As expected, the co-expression of GFP-cGAS with STING induced cytokine (*ifn-β*, *isg54*) expression (Fig. 7E). However, the additional expression of OASL p59 markedly depressed cytokine expression, while the OASL p30 did not impact cytokine levels. We next explored the possible immune-modulatory role of this interaction during HSV-1 infection. We chose to infect cells with *d106* HSV-1, given the ability of this strain to induce cGAS-mediated immune signaling. Upon infection of cells co-expressing cGAS and OASL p59 with *d106*, we observed a similar *ifn-β* depression (Fig. 7F).

Next, we conducted CRISPR-Cas9-mediated knockdown of cGAS and OASL separately in HFFs and assessed both cytokine levels and virus titers upon *d106* HSV-1 infection. We confirmed knockdowns of cGAS and OASL by PRM (Figs. S5A and S5B). For OASL, the single guide RNA (sgRNA) 2 appeared most effective in reducing OASL protein expression, so we proceeded with this cell line. We assessed levels of phospho-IRF3 and phospho-TBK1 by Western blotting (Figure S5C). Compared to control cells (CRISPR-sgScrambled), we saw decreases in these immune signaling markers in cells lacking cGAS (CRISPR-sgcGAS) and increases in cells lacking OASL (CRISPR-sgOASL). Upon assessing virus progeny production, compared to control CRISPR-sgScrambled cells, we observed a significant increase in *d106* progeny production in CRISPR-sgcGAS cells and a significant decrease in CRISPR-sgOASL cells (Fig. 7G).

cGAS has previously been shown to have antiviral effects against several RNA viruses (Schoggins et al., 2014). These findings and our observed negative regulation of cGAS by

OASL prompted us to ask whether the cGAS-OASL interaction also acts in a reciprocal manner to impact immune signaling in the presence of foreign RNA. Upon transfection of poly(I:C) in cells co-expressing cGAS and OASL, we did not find a significant effect of cGAS on OASL-mediated *ifn-β* expression (Fig. 7H). Altogether, when considering the DNA and RNA sensing pathways, our findings implicate a unidirectional role for OASL in suppressing cGAS-mediated cytokines. Within DNA sensing, this interaction may directly, or indirectly, confer a replicative advantage to the *d106* HSV-1 virus. Considering the stability of this interaction in resting cells, our results suggest that it functions as a mechanism to negatively regulate cGAS-dependent cytokine induction during innate immune signaling (Fig. 7I).

Concluding remarks

To maintain a balanced and healthy state, the mammalian innate immune system relies on the coordinated regulation of its immune-modulatory receptors. Here, we tackle the question of how the integral viral DNA sensor, cGAS, is inactively maintained in resting cells and how it is regulated during active immune signaling upon viral infection. By combining protein interactions with quantitative temporal proteome profiling during different HSV-1 infections, we built a resource for investigating the dynamic interplay among homeostatic maintenance of immunity, activation of immune signaling pathways, and mechanisms of viral immune evasion. Our comparison of infections with HSV-1 WT, *d106*, and *d109* strains provide knowledge of alterations in the cellular proteomic landscape during different levels of cytokine induction or apoptosis. Our interactome further serves as an integral roadmap to investigate cellular and viral proteins involved in fine-tuning mechanisms that either homeostatically maintain cytoplasmic cGAS activity or regulate cGAS upon DNA stimulation. Such cGAS protein interactions may affect the ability of cGAS to bind to viral DNA, produce cGAMP, or promote the clearance of cGAMP in immune-stimulated cells. Recently, it was demonstrated that cGAS-mediated immune signaling is activated upon binding the cellular receptor, NONO, during HIV-2 infection (Lahaye et al., 2018). As such, explorations into nuclear cGAS interactions during immune activation also warrant further research.

Our integrative analysis of cGAS interactions and connected proteome changes highlighted an enriched interaction between two immune-modulating factors, cGAS and OASL. We show that this cGAS-OASL association is consistent across different cell types—primary fibroblasts, differentiated monocytes, and epithelial HEK293T cells. Furthermore, this interaction is sustained in mock-treated cells and during exogenous DNA stimulation with either HSV-1 infection or VACV 70mer DNA transfection. Our follow-up analyses determine that this interaction can be facilitated via the OAS-like domain of OASL and the highly-conserved Mab21 domain of cGAS. In assessing the functional impact of this association, we identified that the OASL UBL domains, in coordination with the OAS-like domain, reduce cGAS- and STING-dependent cytokine expression upon DNA stimulation. The fact that OASL p30 was not found to have a functional effect may not be surprising, when considering that p59 is the dominant isoform (Choi et al., 2015). Of note, we observed an enriched interaction of cGAS with OASL during WT HSV-1 infection, relative to infection with HSV-1 strains (*d106* or *d109*) that induce higher cytokine expression levels.

This observation is consistent with our findings that OASL negatively regulates cGAS-dependent cytokine expression. We propose a possible model in which cGAS is maintained in an inactive state during cellular homeostasis in-part through its physical association with OASL (Fig. 7I).

Our OASL-cGAS observations are supported by accounts in the literature of a functional interaction (Leisching et al., 2017), but to our knowledge, our work provides the only reported manuscript containing experimental data to support this functional relationship. Consistent with this finding, loss of the possible mouse homolog, OASL1, in murine immune cell types was previously shown to facilitate immunity against HSV-2 infection (Oh et al., 2016). During latent KSHV reactivation, it was found that OASL promoted viral replication via a co-opted interaction with the viral ORF20 protein (Bussey et al., 2018). Another report concluded that OASL p59 did not affect HSV-1 replication (Marques et al., 2008). Considering these reports, our finding that OASL deficiency enhanced *d106* HSV-1 progeny production may indicate that OASL indirectly promotes HSV-1 replication only under contexts of strong active immune signaling.

Outside of DNA sensing, OASL during RNA sensing activates RIG-I, and thus downstream cytokine expression. In contrast, our findings as a whole suggest a potential homeostatic role for OASL in DNA sensing, redirecting our understanding of what has previously been defined as distinct RNA and DNA sensing pathways. In this way, OASL may play different roles in the canonical mammalian RNA and DNA sensing pathways. We envision that this regulatory crosstalk between these pathways will incite future research in establishing functional relationships among immune-modulatory proteins in contexts pertaining not only to viral infection, but also to disease states with IFN signatures.

STAR Methods

Lead Contact for Reagent and Resource Sharing

Further information and requests for reagents may be directed to, and will be fulfilled by the corresponding author, Ileana M. Cristea (icristea@princeton.edu).

Experimental Model and Subject Details

Cell models—Primary human foreskin fibroblasts (HFFs) and HEK293Ts were cultured in Dulbecco's modified Eagle medium with 10% fetal bovine serum and kept at 37°C in a 5% CO2 environment. HFFs were generously provided by Dr. Hillary Coller (University of California Los Angeles, Los Angeles, CA, USA).

THP-1 monocytes (gift from Dr. Thomas Shenk, Princeton University, Princeton, NJ, USA) were cultured in Roswell Park Memorial Institute 1640 medium (Life Technologies) with 10% fetal bovine serum and 1% penicillin-streptomycin and kept at 37°C in a 5% CO2 environment. For experimentation, THP-1 monocytes were differentiated with 1 μg/mL phorbol 12-myristate 13-acetate (PMA; Sigma Aldrich) for 48h.

Viral Strains and Titers—WT HSV-1 was generated using the bacterial artificial chromosome (BAC) with the full HSV-1 (17+ strain) genome carried by E. coli strain

GS1783, which was a gift from Dr. Beatte Sodeik (Hannover Medical School, Hannover, Germany). The pBAC-HSV-1 was electroporated into Vero cells to harvest P0 WT HSV-1.

The *d106* and *d109* HSV-1 and the respective complementing E11 and F06 (Vero) cells were gifts from Dr. Neal DeLuca of University of Pittsburgh (Pittsburgh, PA, USA). To produce progeny viruses, the cells were infected with virus (MOI 0.001), and the cells and media were collected when 100% cytopathic effect was observed. The media was concentrated by ultracentrifugation at 20,000 rpm for 2 hours at 4°C, and the viruses were resuspended in MNT buffer (200 mM MES, 30mM Tris-HCl, 100 mM NaCl, pH 7.4). To collect cell-associated virus, the infected cells were resuspended in MNT buffer. The cell-free and cell-associated viruses were combined and kept at −80°C until use. Virus titers were acquired by plaque assay on the respective cell types used for propagation. Virus was diluted in DMEM containing 2% (v/v) FBS at the indicated MOI. Virus was added to cell monolayers for 1 h at 37°C with intermittent rocking. After adsorption of virus, cells were washed with PBS, supplemented with DMEM containing 10% FBS, and incubated for the indicated time period.

Method Details

Antibodies—For Western blotting and immunofluorescence microscopy, the following antibodies were used: α-cGAS (MB21D1) (HPA031700; Sigma), α-GFP (#11814460001; Roche), α-FLAG (M2) (F3165; Sigma), α-OASL (ab191701; Abcam), α-tubulin (T6199; Sigma-Aldrich), α-STING (TMEM173) (ab92605; Abcam), α-Phosph.-TBK1 (Ser172) (#5483; Cell Signal Technology), α-TBK1 (#3013; Cell Signaling Technology), α--IRF3 (#4302; Cell Signaling Technology), α-phospho-IRF3 (Ser396) (#4947; Cell Signaling Technology), α-ICP0 (H1A027–100; Virusys Corporation), α-PARP (#9542; Cell Signaling Technology), anti-ASCC3 (ab168810; Abcam), anti-OAS2 (MAB1925; R & D Systems). The secondary antibodies used for immunofluorescence microscopy and the LI-COR Odyssey Western blotting imaging system were conjugated with Alexa Fluor fluorophores (Life Technologies).

Generation of over-expressing and CRISPR-Cas9 cell lines—EGFP-tagged cGAS constructs were generated by overlap-extension PCR and ligated into pcDNA3.1 between the *KpnI* and *XhoI* restriction sites. To generate doxycycline-inducible cell lines, cGAS-EGFP, EGFP-cGAS, and EGFP sequences were subcloned into LentiORF pLVX-TetOne-Puro vector (Open Biosystems). HA-hSTING (THP-1) was a gift from Dr. Russel Vance (University of California Berkley). pcDNA4- FLAG-OASL p30 and -FLAG-OASL p59 were a gift from Dr. Alexei Korennykh (Princeton University). Doxycyline-induced plasmid expression was achieved by adding doxycycline to cells in culture at 1 μg/ml. LentiCRISPRv2 was a gift from Dr. Feng Zhang (Broad Institute of MIT and Harvard; Addgene plasmid # 52961) (Sanjana et al., 2014). Candidate 20 bp sgRNA sequences were designed using the CRISPR Design Tool (http://crispr.mit.edu/). All the CRISPR constructs were generated by inserting the 20 bp sgRNA sequence into the *BsmBI* restriction site.

Construction of HEK293T-STING cells has been previously described (Diner et al., 2016). To construct doxycycline-inducible HFF and HEK293T-STING cells expressing EGFP,

EGFP-cGAS or cGAS-EGFP, cells were transduced with lentivirus generated from pLVX-TetOne-Puro carrying the aforementioned genes for three days. To generate cells expressing CRISPR/Cas9/sgRNA cassettes, the cells were transduced with lentivirus derived from the LentiCRISPRv2 vector containing the respective sgRNA sequences. All lentivirus-transduced cell lines were selected in 2 μg/ml puromycin for one week. Prior to experimentation, the expression of EGFP, EGFP-cGAS, and cGAS-EGFP were induced with doxycycline (1 μg/ml for EGFP, 2 μg/ml for EGFP-cGAS or cGAS-EGFP) for 36 hours.

Plasmid, VACV 70mer, and poly(I:C) Transfections—For packaging lentiviruses in HEK293T cells, X-tremeGENE HP transfection reagent was used according to the manufacturer's protocol. Poly(I:C)- Low molecular weight/LyoVec (Invivogen) was co-transfected with the indicated plasmids into cells at 1 μg/ml according to the manufacturer's protocol for 24 h prior to RNA isolation. For other transfection experiments, including VACV 70mer transfection, Lipofectamine 2000 (Life Technologies) was used according to the manufacturer's protocol. Where indicated in co-transfection experiments to assess cytokines, forward and reciprocal co-IPs, and protein abundances by Western blot, respective empty vectors were used in control samples.

Lentivirus generation—All lentiviruses were packaged and collected from HEK293Ts. The lentivirus transfer vector was co-transfected with lentivirus packaging vectors psPAX2 (packaging) and pMD2.G (envelope) into HEK293Ts, in a ratio of 1:1.5:1 (packaging: envelope: transfer vector). X-tremeGENE HP DNA transfection reagent (Roche) was used in a 2:1 ratio with DNA. Lentiviruses were collected at 40, 56, and 72 hours post-transfection in 30% FBS DMEM, filtered using a 0.45 μm membrane, and stored at −80°C until use.

RNA isolation and qRT-PCR—Cellular RNA was isolated using the RNeasy Mini kit (Qiagen). DNaseI (Invitrogen) was used to digest DNA contaminants. The reverse transcription step was done using RETROscript Reverse Transcription kit (Life Technologies) and SuperScript IV First-Strand Synthesis kit (ThermoFisher Scientific) following the manufacturer's protocols. Quantitative PCR was conducted on the AB7900HT and ViiA 7 real-time PCR systems (Applied Biosystems), using SYBR green PCR master mix (Life Technologies) and gene specific primers. The ΔΔCt method was applied to quantify the relative mRNA abundance of each gene using β-actin as the internal reference.

Western blotting—Cells were lysed in 1x Laemlli sample buffer (62.5 mM Tris-HCL, pH 6.8, 2% SDS (w/v), 10% glycerol (v/v), 0.02% bromophenol blue (w/v), 100 mM DTT) and boiled at 95°C for 10 minutes before running SDS-PAGE. The proteins were blotted onto PVDF membrane by a wet transfer method, and then blocked with 5% (w/v) milk in phosphate-buffered saline (PBS) and incubated with primary and secondary antibodies. Film was exposed using ECL Western Blotting Detection Reagents (GE Healthcare) and immunofluorescence detection was performed using the LI-COR Odyssey CLx imaging system.

Immunocytochemistry and Fluorescence Imaging—Cells for fluorescence imaging experiments were seeded onto number 1.5 glass bottom dishes, one day prior to experimental manipulations. Following indicated virus infections and lengths of time, cells

were fixed in 2% (v/v) paraformaldehyde in PBS for 15 min and permeabilized with 0.1% (v/v) Triton-X 100 in PBS for 15 min. Cells were blocked for 1 hr at RT with 2% (w/v) BSA and 2.5% (v/v) human serum in PBS containing 0.2% Tween 20 (PBS-T). Cells were sequentially incubated with primary and secondary antibodies diluted in PBS-T, and nuclei were stained with 1 μg/ml 4,6-diamidino-2-phenylindole for 10 min. Secondary antibodies were conjugated to either Alexa Fluor 488, or 568 (Life Technologies). Imaging was conducted on a Nikon Spinning Disc TI-E microscope (Orca Flash charge-coupled-device camera [Hamatsu]) and Perfect Focus system using either the 100x objective. Image analysis was conducted with NIS-Elements software (Nikon) and ImageJ (Schindelin et al., 2012).

Cytoplasmic Fractionation and IP—Cells were either infected (MOI 5, 6 hpi) or transfected and then washed and scraped off the plates in PBS. After a 5 min centrifugation at 250 × g, the cells were lysed in cytoplasmic lysis buffer (20 mM HEPES, pH 7.4, 10 mM KCl, 2 mM MgCl2, 1 mM DTT, 0.5% (v/v) NP-40, 1/100 protease inhibitor cocktail (PIC, Sigma), and 1/100 phosphatase inhibitor cocktail (PhIC, Sigma)) for 30 min on ice, with vortexing every 5 min. The lysate was centrifuged at 1000 × g for 10 min to separate the cytoplasmic fraction from the nuclear pellet. The nuclear pellet was lysed (cytoplasmic lysis buffer supplemented with 200 mM NaCl, 1% (v/v) Triton X-100, 0.11 M KOAc, 1% (v/v) Tween-20), and then centrifuged at 1000 × g for 10 min to clarify the lysates. To limit the identification of indirect interactions mediated by DNA, 100 U of the endonuclease Benzonase (Pierce) was added to each fraction, and the lysates were incubated at RT for 10 min. Immunoaffinity purification was subsequently conducted by adding 5 mg Dynabeads Magnetic Beads (M270, ThermoFisher Scientific) conjugated with α-GFP antibody (in-house generated; 5 μg antibody/mg magnetic beads) to the fractionated lysates and incubated for 1 hr at 4°C with end-over-end rotation. Antibody-conjugated magnetic beads were prepared as previously described (Diner et al., 2015, Diner et al., 2016, Luo et al., 2010). Following the IP, beads were washed six times with lysis buffer and once with PBS, and then protein complexes were eluted by incubating the beads in 1x Laemlli sample buffer at 70°C for 10min. The eluates were then reduced with 25 mM TCEP (ThermoFisher Scientific) and analyzed by Western blotting or prepared for mass spectrometry.

Sample Preparation and Mass spectrometry—IP eluates were alkylated with 50 mM chloroacetamide (CAM), and then separated on a NuPAGE 4–12% Bis-Tris gel (Invitrogen). After Coomassie blue staining and destaining with water, whole gel lanes were digested with trypsin (Promega) as previously described (Diner et al., 2015). Desalting was then conducted using StageTips with SDB-RPS membrane. The resulting peptides were analyzed by LC-MS/MS on an LTQ Orbitrap Velos (Thermo Scientific) for the HEK 293T-STING cells as previously described (Diner et al., 2016), or on a Q Exactive HF Hybrid Quadrupole-Orbitrap (Thermo Scientific) for the HFFs. IP samples analyzed on the Q Exactive were chromatographically resolved on an EASYSpray C18 column (75μm × 25cm) over a linear gradient of solvents A (0.1% FA in H_2O) and B (0.1% FA, 2.9% H_2O in ACN) from 3% B to 37% B over 60 min at a flow rate of 250 nL/min. Peptides were ionized at 1.7 kv and an MS1 scan was performed from 350 to 1800 *m/z* at 120,000 resolution with an automatic gain control (AGC) setting of 3e6 and a maximum injection time (MIT) of 30 ms recorded in profile. The top 15 precursors were then selected for fragmentation and MS2 scans were

acquired at a resolution of 15,000 with an AGC setting of 1e5, an MIT of 42 ms, an isolation window of 1.2 *m/z*, a fixed first mass of 100 *m/z*, normalized collision energy of 28, peptide match set to preferred, and a dynamic exclusion of 25 s recorded in centroid.

Whole proteome LC-MS/MS.—Cell pellets were lysed in 2% SDS, 100 mM NaCl, 0.5 mM EDTA, 50 mM Tris, pH 8.2, and 100 μg of protein was reduced and alkylated with 25mM TCEP and 50mM CAM respectively for 20 min at 70°C and then digested overnight with trypsin (50:1 protein:enzyme w/w ratio) in 50 mM HEPES, pH8.2. Digested samples were concentrated by speed vac to one half the original volume and adjusted to a final concentration of 20% acetonitrile (ACN). Both biological replicates for WT and d106 viruses were labeled concurrently with a 10-plex TMT kit (Thermo Fisher Scientific). The TMT reagents were dissolved in anhydrous ACN and 0.2mg of reagent from each channel was added to the appropriate sample for 1 hr at RT. To quench the reaction, hydroxylamine was added to a final concentration of 0.5% (v/v) and the samples were incubated at RT for 15 min. Labeled peptides were pooled at equal peptide amounts to generate each 10-plex experiment.

Peptide fractionation.—Pooled peptides were first desalted via C18 StageTips to remove unreacted TMT reagent. Bound peptides were washed with 5% ACN, 0.5% formic acid (FA) and then eluted in 70% ACN, 0.5% FA. The eluted peptides were then fractionated using SCX StageTips and sequentially eluted (100 μL) as follows: (1) 0.05 M ammonium formate/20% ACN, (2) 0.05 M ammonium acetate/20% ACN, (3) 0.05 M ammonium bicarbonate/20% ACN, and (4) 0.1% ammonium hydroxide/20% ACN. Each of these fractions was diluted 1:1 with 1% trifluoroacetic acid and further fractionated by SDB-RPS StageTips into three fractions (50 μL elutions) as follows: (1) 0.2 M ammonium formate/ 0.5% FA/60% ACN, (2) 0.2 M ammonium acetate/0.5% FA/60% ACN, (3) 5% ammonium hydroxide/80% ACN. The final 12 fractions for each 10-plex experiment were dried via speed vac and resuspended in 5 μL of 1% FA, 1% ACN in water.

LC-MS/MS for TMT analysis.—Peptides (2 μL) from each fraction were analyzed using a Dionex Ultimate 3000 UHPLC coupled online to an EASYSpray ion source and a Q Exactive HF. Peptides were separated on an EASYSpray C18 column (75μm × 25cm) heated to 50°C using a gradient of 6% B to 18% B over 100 min and then to 29% B over 50 min at a flow rate of 250 nL/min. Peptides were ionized at 1.7 kv and an MS1 scan was performed from 350 to 1800 *m/z* at 120,000 resolution with an AGC setting of 3e6 and an MIT of 30 ms recorded in profile. The top 20 precursors were then selected for fragmentation and MS2 scans were acquired at a resolution of 45,000 with an AGC setting of 1e5, an MIT of 72 ms, an isolation window of 1.2 *m/z*, a fixed first mass of 100 *m/z*, normalized collision energy of 34, peptide match set to preferred, and a dynamic exclusion of 30 s recorded in profile.

Targeted quantification by PRM.—Cell pellets were lysed in 2% SDS, 100 mM NaCl, 0.5 mM EDTA, 50 mM Tris, pH 8.2, and 50 μg of protein was reduced and alkylated with 25mM TCEP and 50mM CAM respectively for 20 min at 70°C and then digested overnight with trypsin (50:1 protein:enzyme w/w ratio) in 50 mM HEPES, pH8.2. Peptides (1.5 μg on column) were analyzed by LC-MS/MS using the same system described above. Peptides

were separated via the following gradient: 4%B to 14% B over 40 min and then to 25% B over 20 min. The PRM method was controlled by a peptide inclusion list with retention time windows of 5 min for selected precursor ions. The PRM method consisted of MS2 scans that were acquired at a resolution of 45,000 with an AGC setting of 5e5, an MIT of 500 ms, an isolation window of 0.8 *m/z*, fixed first mass of 125.0 *m/z*, and normalized collision energy of 27 recorded in profile.

Quantification and Statistical Analysis

cGAS interaction network assembly—Specificity filtering on weighted spectral counts was conducted using the SAINT (Significance Analysis of INTeractome) algorithm (Choi et al., 2011), and a value of 0.90 was used as a specificity threshold for the IPs conducted in the HFF cells and 0.95 for the IPs conducted in HEK293T-STING cells (see Fig. S2 in the supplemental material). The CRAPome repository (Mellacheruvu et al., 2013) was used to further remove non-specific protein interactors. The CRAPome database is a repository of proteins identified in the IPs of negative control isolations conducted under a large range of experimental conditions. Proteins with greater than 20% appearance in the CRAPome database were removed from the finalized cGAS interaction lists (Tables S1–S2). Spectral counts were normalized to the relative amounts of cGAS bait captured. The specificity-filtered proteins were submitted to the STRING database (Szklarczyk et al., 2017, Szklarczyk et al., 2011) and categorized by Gene Ontology. Through STRING, network edges were incorporated from a combination of evidence sources, including previously published experiments, databases, co-expression data, conserved neighborhood occurrences, gene fusion events, and co-occurrences across species. To further enrich for cytoplasmic cGAS interactions and to maintain stringent filtering, proteins that were reported to localize solely to the nucleus were removed from the dataset (Table S1). The remaining proteins were assembled into an interaction network visualized in Cytoscape (v. 3.5.1) (Shannon et al., 2003). To provide a visualization of relative enrichment among the cGAS-interacting proteins, we calculated the maximum normalized spectral abundance factors (NSAF; (Zybailov et al., 2006)) for each protein in our cGAS interaction network. This factor is representative of the highest enrichment achieved for that protein in either the Mock or HSV-1-infected conditions and allows for direct comparison of the enrichment values of different proteins. For ease of visualization, the resulting NSAF values were all scaled by 1e6 and then $\log_2$ transformed. The resulting NSAF values were then depicted in the Cytoscape network as the color of the border around each node.

Quantitative analysis of PRM data—Label-free targeted quantitation of peptides specific for proteins of interest was designed and analyzed using the Skyline software. Summed area under the curve of 3–4 transitions per peptide was used for quantitation. Targeted peptides were normalized to two loading control peptides: EDMAALEK from tubulin and LEVNLQAMK from myosin-9. PRM quantitation data were graphed in GraphPad Prism v5.04. For reciprocal IP PRMs, cGAS peptides were normalized to peptides from the bait proteins.

Bioinformatic analysis of MS data—MS/MS data were analyzed by Proteome Discoverer (Thermo Fisher Scientific, v1.4 for IP-MS experiments and v2.2 for PRM and

TMT experiments). The spectra were searched against a Uniprot human database containing herpesvirus sequences and appended with common contaminants (2016–04, 22,349 sequences). The search required fully tryptic peptides, 5 ppm precursor mass accuracy, and a fragment ion mass accuracy of 0.02 Da for Q Exactive data and 0.3 Da for Orbitrap Velos data. Allowed peptide modifications included static carbamidomethylation on cysteine, dynamic oxidation on methionine, dynamic deamidation on asparagine, dynamic phosphorylation on serine, threonine, and tyrosine, dynamic methionine loss and acetylation on protein n-termini, and static TMT additions on peptide N-termini and lysine residues for the TMT experiments. All matched spectra were scored by Percolator, PTMs were localized by ptmRS, and for the TMT data, reporter ion signal-to-noise (S/N) values were extracted. The resulting peptide spectrum matches were parsimoniously assembled into peptide and protein identifications with a false discovery rate of less than 1% for both the peptide and protein level with at least 2 unique peptides identified per protein. For the IP data, this final assembly was performed in Scaffold (Proteome Software, v4.7.3) and for the TMT data, this was performed in Proteome Discoverer 2.2. TMT reporter ion quantification for unmodified unique and razor peptides was performed with a requirement for an average S/N of at least 10 and precursor co-isolation thresholds of less than 30%. Reporter ion values were normalized to the sum of the detected signal in each channel. Protein abundances were calculated per channel as the sum of all normalized reporter ion values for each peptide in each protein. Missing values were imputed using the low abundance resampling algorithm. Statistically differential proteins were assessed via a background-based ANOVA analysis implemented in Proteome Discoverer. Proteins and associated TMT reporter ion abundances were exported to Excel for further analysis. Differential proteins (adjusted p-value ≤ 0.05) were analyzed via over representation analysis (www.pantherdb.org and DAVID bioinformatics database v.6.8) for associated gene ontology enrichments. For the TMT proteins identified and classified as positive regulators of either apoptosis or innate immunity, proteins were filtered to include proteins that either exhibit the highest fold-changes (Infection/Mock), or are prominent markers of these functional classes. Heatmaps of TMT and IP data were generated using Morpheus (Broad Institute).

Data Availability

The mass spectrometry proteomics data have been deposited to the ProteomeXchange Consortium via the PRIDE partner repository (Vizcaino et al., 2016) with the dataset identifier PXD010162.

Supplementary Material

Refer to Web version on PubMed Central for supplementary material.

Acknowledgments

We thank Dr. Todd Greco for MS analysis assistance. Funding was provided by NIH, NIGMS grant GM114141 and by the Edward Mallinckrodt Foundation to I.M.C., NIH fellowship F31GM120936 to K.K.L, CSC scholarship 201506210052 to B.S., and AHA fellowship 14PRE18890044 to B.A.D.

References

Aguirre S, Luthra P, Sanchez-Aparicio MT, Maestre AM, Patel J, Lamothe F, Fredericks AC, Tripathi S, Zhu T, Pintado-Silva J, et al. (2017). Dengue virus NS2B protein targets cGAS for degradation and prevents mitochondrial DNA sensing during infection. Nat. Microbiol 2, 17037. [PubMed: 28346446]

Bussey KA, Lau U, Schumann S, Gallo A, Osbelt L, Stempel M, Arnold C, Wissing J, Gad HH, Hartmann R, et al. (2018). The interferon-stimulated gene product oligoadenylate synthetase-like protein enhances replication of Kaposi's sarcoma-associated herpesvirus (KSHV) and interacts with the KSHV ORF20 protein. PLOS Pathog. 14, e1006937. [PubMed: 29499066]

Chattopadhyay S, Marques JT, Yamashita M, Peters KL, Smith K, Desai A, Williams BRG & Sen GC (2010). Viral apoptosis is induced by IRF-3-mediated activation of Bax. EMBO J. 29, 1762–1773. [PubMed: 20360684]

Chen M, Meng Q, Qin Y, Liang P, Tan P, He L, Zhou Y, Chen Y, Huang J, Wang RF, et al. (2016). TRIM14 Inhibits cGAS Degradation Mediated by Selective Autophagy Receptor p62 to Promote Innate Immune Responses. Mol. Cell 64, 105–119. [PubMed: 27666593]

Choi H, Larsen B, Lin ZY, Breitkreutz A, Mellacheruvu D, Fermin D, Qin ZS, Tyers M, Gingras AC & Nesvizhskii AI (2011). SAINT: probabilistic scoring of affinity purification-mass spectrometry data. Nat. Methods 8, 70–U100. [PubMed: 21131968]

Choi UY, Kang JS, Hwang YS & Kim YJ (2015). Oligoadenylate synthase-like (OASL) proteins: dual functions and associations with diseases. Exp. Mol. Med 47, e144. [PubMed: 25744296]

Cristea IM, Williams R, Chait BT & Rout MP (2005). Fluorescent proteins as proteomic probes. Mol. Cell. Proteomics 4, 1933–41. [PubMed: 16155292]

Diner BA, Lum KK, Javitt A & Cristea IM (2015). Interactions of the Antiviral Factor Interferon Gamma-Inducible Protein 16 (IFI16) Mediate Immune Signaling and Herpes Simplex Virus-1 Immunosuppression. Mol. Cell. Proteomics 14, 2341–56. [PubMed: 25693804]

Diner BA, Lum KK, Toettcher JE & Cristea IM (2016). Viral DNA Sensors IFI16 and Cyclic GMP-AMP Synthase Possess Distinct Functions in Regulating Viral Gene Expression, Immune Defenses, and Apoptotic Responses during Herpesvirus Infection. MBio 7.

Diner EJ, Burdette DL, Wilson SC, Monroe KM, Kellenberger CA, Hyodo M, Hayakawa Y, Hammond MC & Vance RE (2013). The innate immune DNA sensor cGAS produces a noncanonical cyclic dinucleotide that activates human STING. Cell Rep. 3, 1355–61. [PubMed: 23707065]

Gao D, Wu J, Wu YT, Du F, Aroh C, Yan N, Sun L & Chen ZJ (2013). Cyclic GMP-AMP synthase is an innate immune sensor of HIV and other retroviruses. Science 341, 903–6. [PubMed: 23929945]

Hornung V, Hartmann R, Ablasser A & Hopfner KP (2014). OAS proteins and cGAS: unifying concepts in sensing and responding to cytosolic nucleic acids. Nat. Rev. Immunol 14, 521–8. [PubMed: 25033909]

Jerome KR, Fox R, Chen Z, Sears AE, Lee HY & Corey L (1999). Herpes simplex virus inhibits apoptosis through the action of two genes, Us5 and Us3. J. Virol 73, 8950–8957. [PubMed: 10516000]

Kulej K, Avgousti DC, Sidoli S, Herrmann C, Della Fera AN, Kim ET, Garcia BA & Weitzman MD (2017). Time-resolved Global and Chromatin Proteomics during Herpes Simplex Virus Type 1 (HSV-1) Infection. Mol. Cell. Proteomics 16, S92–S107. [PubMed: 28179408]

Lahaye X, Gentili M, Silvin A, Conrad C, Picard L, Jouve M, Zueva E, Maurin M, Nadalin F, Knott GJ, et al. (2018). NONO Detects the Nuclear HIV Capsid to Promote cGAS-Mediated Innate Immune Activation. Cell 175, 488–501 e22. [PubMed: 30270045]

Langelier Y, Bergeron S, Chabaud S, Lippens J, Guilbault C, Sasseville AM, Denis S, Mosser DD & Massie B (2002). The R1 subunit of herpes simplex virus ribonucleotide reductase protects cells against apoptosis at, or upstream of, caspase-8 activation. J. Gen. Virol 83, 2779–89. [PubMed: 12388814]

Lee MS, Kim B, Oh GT & Kim YJ (2013). OASL1 inhibits translation of the type I interferon-regulating transcription factor IRF7. Nat. Immunol 14, 346–55. [PubMed: 23416614]

Leisching G, Wiid I & Baker B (2017). The Association of OASL and Type I Interferons in the Pathogenesis and Survival of Intracellular Replicating Bacterial Species. Front. Cell. Infect. Microbiol 7, 196. [PubMed: 28580319]

Li J, Ding SC, Cho H, Chung BC, Gale M, Jr., Chanda SK & Diamond MS (2013a). A short hairpin RNA screen of interferon-stimulated genes identifies a novel negative regulator of the cellular antiviral response. MBio 4, e00385–13. [PubMed: 23781071]

Li T, Diner BA, Chen J & Cristea IM (2012). Acetylation modulates cellular distribution and DNA sensing ability of interferon-inducible protein IFI16. Proc. Natl. Acad. Sci 109, 10558–63. [PubMed: 22691496]

Li X, Shu C, Yi G, Chaton CT, Shelton CL, Diao J, Zuo X, Kao CC, Herr AB & Li P (2013b). Cyclic GMP-AMP synthase is activated by double-stranded DNA-induced oligomerization. Immunity 39, 1019–31. [PubMed: 24332030]

Li XD, Wu J, Gao D, Wang H, Sun L & Chen ZJ (2013c). Pivotal roles of cGAS-cGAMP signaling in antiviral defense and immune adjuvant effects. Science 341, 1390–4. [PubMed: 23989956]

Lian H, Wei J, Zang R, Ye W, Yang Q, Zhang XN, Chen YD, Fu YZ, Hu MM, Lei CQ, et al. (2018). ZCCHC3 is a co-sensor of cGAS for dsDNA recognition in innate immune response. Nat. Commun 9, 3349. [PubMed: 30135424]

Liang QM, Seo GJ, Choi YJ, Kwak MJ, Ge JN, Rodgers MA, Shi MD, Leslie BJ, Hopfner KP, Ha T, et al. (2014). Crosstalk between the cGAS DNA Sensor and Beclin-1 Autophagy Protein Shapes Innate Antimicrobial Immune Responses. Cell Host Micr. 15, 228–238.

Luo Y, Li T, Yu F, Kramer T & Cristea IM (2010). Resolving the composition of protein complexes using a MALDI LTQ Orbitrap. J. Am. Soc. Mass Spectrom 21, 34–46. [PubMed: 19822444]

MacLean B, Tomazela DM, Shulman N, Chambers M, Finney GL, Frewen B, Kern R, Tabb DL, Liebler DC & MacCoss MJ (2010). Skyline: an open source document editor for creating and analyzing targeted proteomics experiments. Bioinformatics 26, 966–8. [PubMed: 20147306]

Marques J, Anwar J, Eskildsen-Larsen S, Rebouillat D, Paludan SR, Sen G, Williams BR & Hartmann R (2008). The p59 oligoadenylate synthetase-like protein possesses antiviral activity that requires the C-terminal ubiquitin-like domain. J. Gen. Virol 89, 2767–72. [PubMed: 18931074]

Mellacheruvu D, Wright Z, Couzens AL, Lambert JP, St-Denis NA, Li T, Miteva YV, Hauri S, Sardiu ME, Low TY, et al. (2013). The CRAPome: a contaminant repository for affinity purification-mass spectrometry data. Nat. Methods 10, 730-+. [PubMed: 23921808]

Mi H, Poudel S, Muruganujan A, Casagrande JT & Thomas PD (2016). PANTHER version 10: expanded protein families and functions, and analysis tools. Nucleic Acids Res. 44, D336–42. [PubMed: 26578592]

Mogensen TH, Melchjorsen J, Malmgaard L, Casola A & Paludan SR (2004). Suppression of proinflammatory cytokine expression by herpes simplex virus type 1. J. Virol 78, 5883–5890. [PubMed: 15140986]

Morchikh M, Cribier A, Raffel R, Amraoui S, Cau J, Severac D, Dubois E, Schwartz O, Bennasser Y & Benkirane M (2017). HEXIM1 and NEAT1 Long Non-coding RNA Form a Multi-subunit Complex that Regulates DNA-Mediated Innate Immune Response. Mol. Cell 67, 387–399 e5. [PubMed: 28712728]

Oh JE, Lee MS, Kim YJ & Lee HK (2016). OASL1 deficiency promotes antiviral protection against genital herpes simplex virus type 2 infection by enhancing type I interferon production. Sci. Rep 6, 19089. [PubMed: 26750802]

Orzalli MH, Broekema NM, Diner BA, Hancks DC, Elde NC, Cristea IM & Knipe DM (2015). cGAS-mediated stabilization of IFI16 promotes innate signaling during herpes simplex virus infection. Proc. Natl. Acad. Sci 112, E1773–81. [PubMed: 25831530]

Orzalli MH, DeLuca NA & Knipe DM (2012). Nuclear IFI16 induction of IRF-3 signaling during herpesviral infection and degradation of IFI16 by the viral ICP0 protein. Proc. Natl. Acad. Sci 109, E3008–17. [PubMed: 23027953]

Paijo J, Doring M, Spanier J, Grabski E, Nooruzzaman M, Schmidt T, Witte G, Messerle M, Hornung V, Kaever V, et al. (2016). cGAS Senses Human Cytomegalovirus and Induces Type I Interferon Responses in Human Monocyte-Derived Cells. PLOS Pathog. 12.

Rebouillat D, Marie I & Hovanessian AG (1998). Molecular cloning and characterization of two related and interferon-induced 56-kDa and 30-kDa proteins highly similar to 2'−5' oligoadenylate synthetase. Eur. J. Biochem 257, 319–30. [PubMed: 9826176]

Samaniego LA, Neiderhiser L & DeLuca NA (1998). Persistence and expression of the herpes simplex virus genome in the absence of immediate-early proteins. J. Virol 72, 3307–20. [PubMed: 9525658]

Sanfilippo CM & Blaho JA (2006). ICP0 gene expression is a herpes simplex virus type 1 apoptotic trigger. J. Virol 80, 6810–6821. [PubMed: 16809287]

Sanjana NE, Shalem O & Zhang F (2014). Improved vectors and genome-wide libraries for CRISPR screening. Nat. Methods 11, 783–784. [PubMed: 25075903]

Schindelin J, Arganda-Carreras I, Frise E, Kaynig V, Longair M, Pietzsch T, Preibisch S, Rueden C, Saalfeld S, Schmid B, et al. (2012). Fiji: an open-source platform for biological-image analysis. Nat. Methods 9, 676–82. [PubMed: 22743772]

Schoggins JW, MacDuff DA, Imanaka N, Gainey MD, Shrestha B, Eitson JL, Mar KB, Richardson RB, Ratushny AV, Litvak V, et al. (2014). Pan-viral specificity of IFN-induced genes reveals new roles for cGAS in innate immunity. Nature 505, 691–5. [PubMed: 24284630]

Seo GJ, Kim C, Shin WJ, Sklan EH, Eoh H & Jung JU (2018). TRIM56-mediated monoubiquitination of cGAS for cytosolic DNA sensing. Nat. Commun 9, 613. [PubMed: 29426904]

Seo GJ, Yang A, Tan B, Kim S, Liang QM, Choi Y, Yuan WM, Feng PH, Park HS & Jung JU (2015). Akt Kinase-Mediated Checkpoint of cGAS DNA Sensing Pathway. Cell Rep. 13, 440–449. [PubMed: 26440888]

Shannon P, Markiel A, Ozier O, Baliga NS, Wang JT, Ramage D, Amin N, Schwikowski B & Ideker T (2003). Cytoscape: a software environment for integrated models of biomolecular interaction networks. Genome Res. 13, 2498–504. [PubMed: 14597658]

Sun L, Wu J, Du F, Chen X & Chen ZJ (2013). Cyclic GMP-AMP synthase is a cytosolic DNA sensor that activates the type I interferon pathway. Science 339, 786–91. [PubMed: 23258413]

Szklarczyk D, Franceschini A, Kuhn M, Simonovic M, Roth A, Minguez P, Doerks T, Stark M, Muller J, Bork P, et al. (2011). The STRING database in 2011: functional interaction networks of proteins, globally integrated and scored. Nucleic Acids Res. 39, D561–8. [PubMed: 21045058]

Szklarczyk D, Morris JH, Cook H, Kuhn M, Wyder S, Simonovic M, Santos A, Doncheva NT, Roth A, Bork P, et al. (2017). The STRING database in 2017: quality-controlled protein-protein association networks, made broadly accessible. Nucleic Acids Res. 45, D362–D368. [PubMed: 27924014]

Vizcaino JA, Csordas A, del-Toro N, Dianes JA, Griss J, Lavidas I, Mayer G, Perez-Riverol Y, Reisinger F, Ternent T, et al. (2016). 2016 update of the PRIDE database and its related tools. Nucleic Acids Res. 44, D447–56. [PubMed: 26527722]

Wang Y, Ning X, Gao P, Wu S, Sha M, Lv M, Zhou X, Gao J, Fang R, Meng G, et al. (2017). Inflammasome Activation Triggers Caspase-1-Mediated Cleavage of cGAS to Regulate Responses to DNA Virus Infection. Immunity 46, 393–404. [PubMed: 28314590]

West AP, Khoury-Hanold W, Staron M, Tal MC, Pineda CM, Lang SM, Bestwick M, Duguay BA, Raimundo N, MacDuff DA, et al. (2015). Mitochondrial DNA stress primes the antiviral innate immune response. Nature 520, 553–7. [PubMed: 25642965]

Wu JJ, Li WW, Shao YM, Avey D, Fu BS, Gillen J, Hand T, Ma SM, Liu X, Miley W, et al. (2015). Inhibition of cGAS DNA Sensing by a Herpesvirus Virion Protein. Cell Host Micr. 18, 333–344.

Wu JX, Sun LJ, Chen X, Du FH, Shi HP, Chen C & Chen ZJJ (2013). Cyclic GMP-AMP Is an Endogenous Second Messenger in Innate Immune Signaling by Cytosolic DNA. Science 339, 826–830. [PubMed: 23258412]

Wu MZ, Cheng WC, Chen SF, Nieh S, O'Connor C, Liu CL, Tsai WW, Wu CJ, Martin L, Lin YS, et al. (2017). miR-25/93 mediates hypoxia-induced immunosuppression by repressing cGAS. Nat. Cell Biol 19, 1286–1296. [PubMed: 28920955]

Xia P, Ye B, Wang S, Zhu X, Du Y, Xiong Z, Tian Y & Fan Z (2016). Glutamylation of the DNA sensor cGAS regulates its binding and synthase activity in antiviral immunity. Nat. Immunol 17, 369–78. [PubMed: 26829768]

Xing J, Ni L, Wang S, Wang K, Lin R & Zheng C (2013). Herpes simplex virus 1-encoded tegument protein VP16 abrogates the production of beta interferon (IFN) by inhibiting NF-kappaB activation

and blocking IFN regulatory factor 3 to recruit its coactivator CBP. J. Virol 87, 9788–801. [PubMed: 23824799]

Yoh SM, Schneider M, Seifried J, Soonthornvacharin S, Akleh RE, Olivieri KC, De Jesus PD, Ruan C, de Castro E, Ruiz PA, et al. (2015). PQBP1 Is a Proximal Sensor of the cGAS-Dependent Innate Response to HIV-1. Cell 161, 1293–1305. [PubMed: 26046437]

Zhang GG, Chan B, Samarina N, Abere B, Weidner-Glunde M, Buch A, Pich A, Brinkmann MM & Schulz TF (2016). Cytoplasmic isoforms of Kaposi sarcoma herpesvirus LANA recruit and antagonize the innate immune DNA sensor cGAS. Proc. Natl. Acad. Sci 113, E1034–E1043. [PubMed: 26811480]

Zhang J, Zhao J, Xu S, Li J, He S, Zeng Y, Xie L, Xie N, Liu T, Lee K, et al. (2018). Species-Specific Deamidation of cGAS by Herpes Simplex Virus UL37 Protein Facilitates Viral Replication. Cell Host Micr. 24, 234–248 e5.

Zhang X, Wu J, Du F, Xu H, Sun L, Chen Z, Brautigam CA, Zhang X & Chen ZJ (2014). The cytosolic DNA sensor cGAS forms an oligomeric complex with DNA and undergoes switch-like conformational changes in the activation loop. Cell Rep. 6, 421–30. [PubMed: 24462292]

Zhu J, Zhang Y, Ghosh A, Cuevas RA, Forero A, Dhar J, Ibsen MS, Schmid-Burgk JL, Schmidt T, Ganapathiraju MK, et al. (2014). Antiviral activity of human OASL protein is mediated by enhancing signaling of the RIG-I RNA sensor. Immunity 40, 936–48. [PubMed: 24931123]

Zybailov B, Mosley AL, Sardiu ME, Coleman MK, Florens L & Washburn MP (2006). Statistical analysis of membrane proteome expression changes in Saccharomyces cerevisiae. J. Proteome Res 5, 2339–47. [PubMed: 16944946]

Highlights

- Defined global network of cytoplasmic cGAS protein interactions upon HSV1 infection
- Mapped the temporal proteomes with IFN- and apoptosis-inducing HSV1 strains
- Oligoadenylate synthase-like domain of OASL associates with cGAS in the cytoplasm
- OASL negatively regulates cGAS-mediated cytokine induction

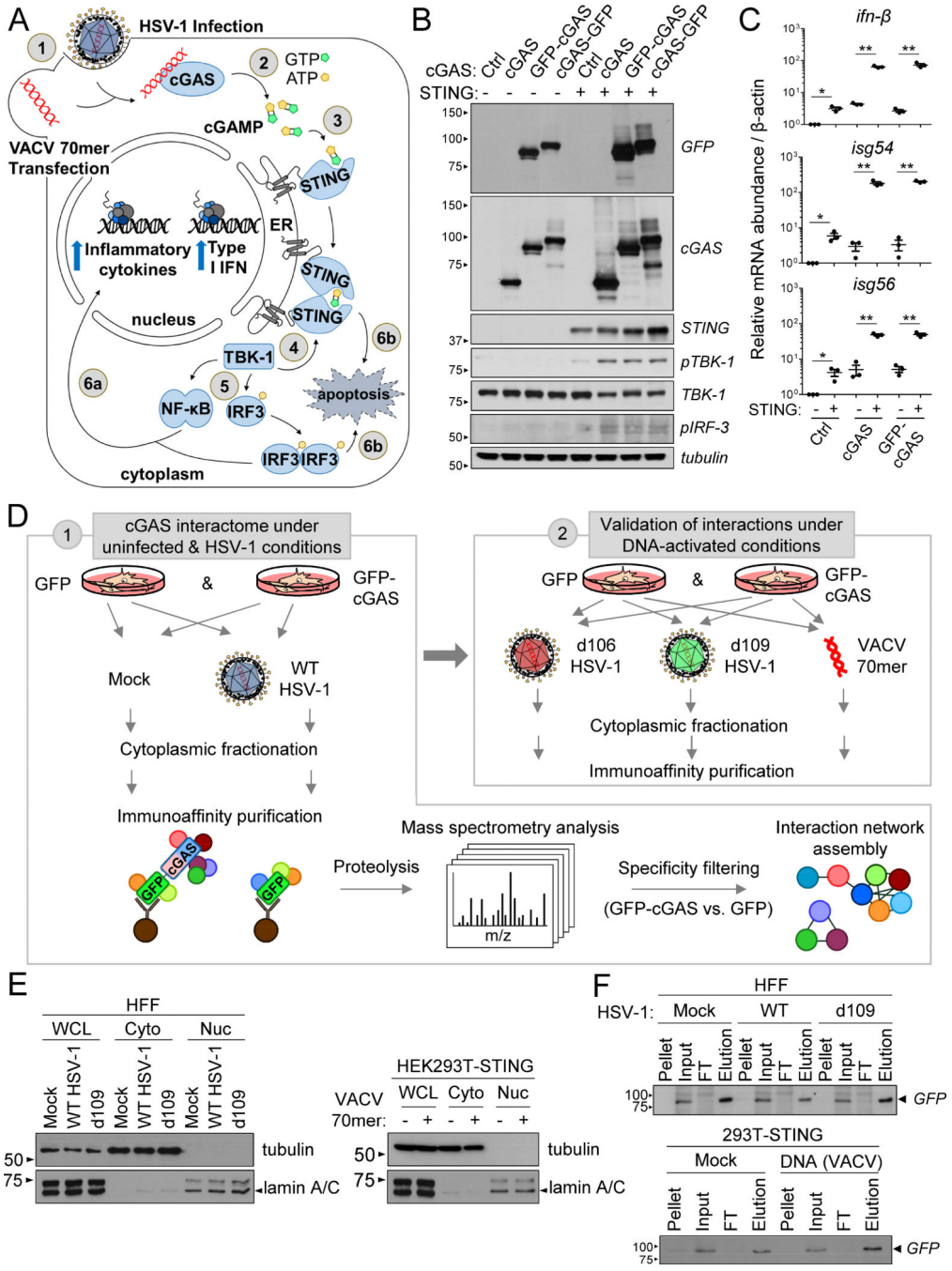

Fig. 1. Development and validation of a platform to characterize cGAS protein interactions during active immune signaling.

(A) The cytoplasmic cGAS-STING pathway senses pathogen-derived DNA and induces cytokines and Type I IFNs. Under certain conditions, pathway activation can also initiate apoptosis.

(B) Protein levels of GFP, cGAS, STING, and phospho-TBK1 were measured by Western blot. HEK293Ts were co-transfected with STING and the GFP-tagged cGAS constructs. See also Figure S1.

(C) Cytokines mRNA levels measured via qPCR in HEK293Ts transiently co-expressing STING with either cGAS or GFP-cGAS. $n = 3$; Error bars= S.E.M. Significantly different values ($P \leq 0.01$) from that of the control are indicated by Student's t test (**).
(D) IP-MS/MS proteomic workflow to characterize cytoplasmic cGAS interactions in HFFs with or without WT HSV-1 infection. Inducible cell lines expressing either GFP-cGAS or free GFP were made in both HFFs and HEK293T-STINGs. Validation experiments were conducted in HFFs infected with *d106* or *d109* HSV-1, and in HEK293T-STINGs either mock- or VACV 70mer-transfected. Proteins found to interact with GFP-cGAS were compared to those found to interact with GFP in mock, HSV-1 infection, and VACV 70mer transfection conditions. See also Figure S1.
(E) Western blots showing efficiency of nuclear-cytoplasmic fractionation in HFFs and HEK293T-STINGs, infected and transfected as in (D), respectively.
(F) Western blots showing efficiency of GFP-cGAS isolation in the cytoplasmic fraction of HFFs and HEK293T-STINGs, infected and transfected as in (D), respectively.

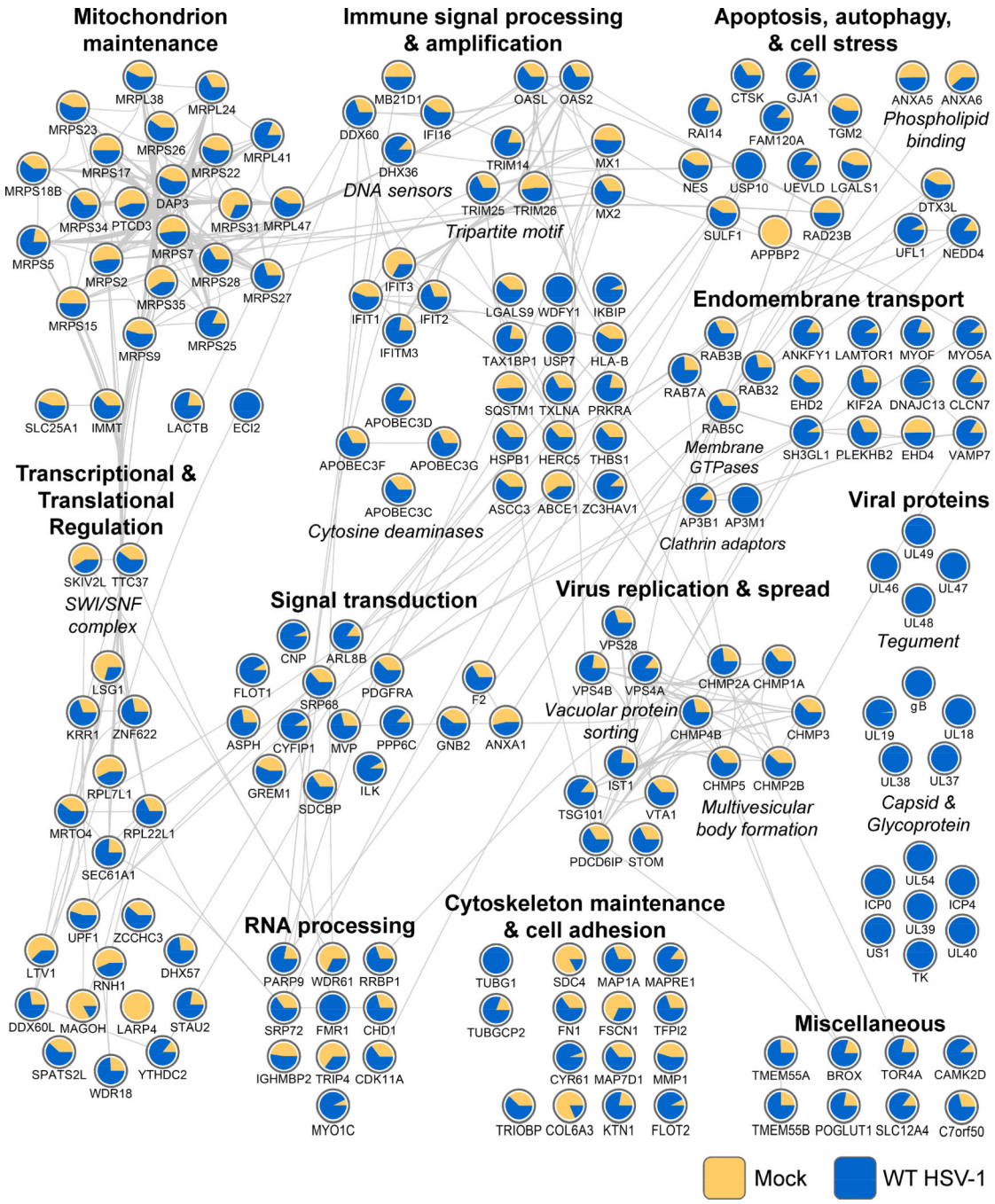

Fig. 2. cGAS differentially interacts with an array of cellular and viral proteins during HSV-1 infection.

Specificity-filtered cGAS interactions were assembled into a functional interaction network. Grey lines depict previously identified interactions with other prey proteins. Pie charts depict relative spectral count enrichment of the protein between mock- (yellow) and WT HSV-1- (blue) infected HFFs (MOI 5, 6 hpi), normalized to cGAS bait levels. See also Figure S2.

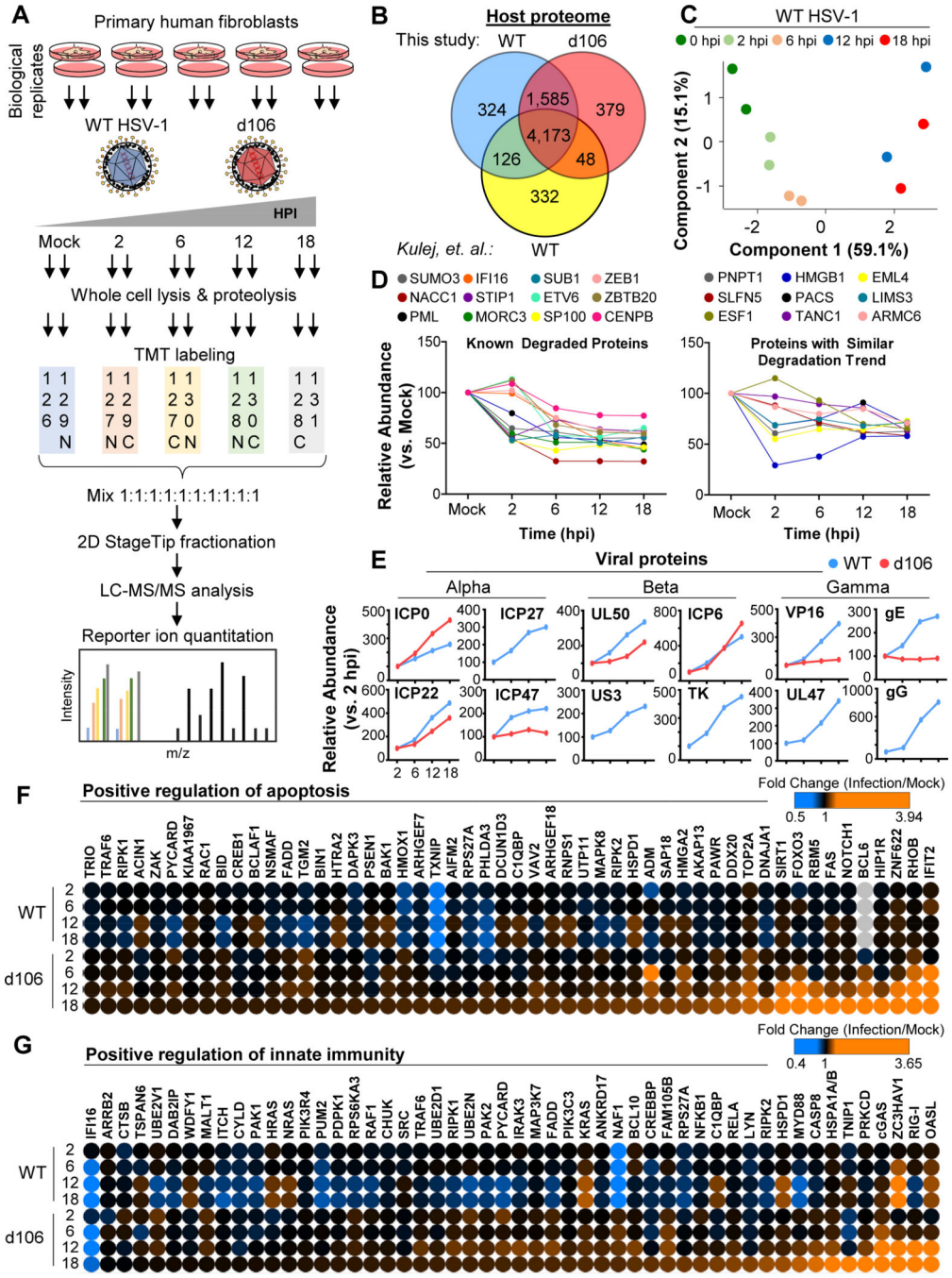

Fig. 3. Temporal proteome alterations during the replication cycle of immune-evasive WT HSV-1 and immune- and apoptosis-stimulatory *d106* HSV-1.

(A) Workflow for time-resolved characterization of the cellular and viral proteome. HFFs were infected (MOI 5) and collected at 0 (mock), 2, 6, 12, and 18 hpi. Quantification of biological replicates was performed by TMT 10plex-labeling and LC-MS/MS.

(B) Numbers of cellular proteins identified in the current study (WT and *d106*) and by (Kulej et al., 2017) (WT).

(C) Principal component analysis of quantified proteins from WT HSV-1 infection experiments (biological replicates). See also Figure S3.

(D) Temporal levels of proteins known to be degraded during infection (left), and proteins that follow simular degradation trends (right), but which remain to be characterized as degraded during infection.

(E) Temporal profiles of selected viral proteins within each HSV-1 gene class.

(F) Temporal profiles of cellular proteins classified as positive apoptosis regulators. The gray BCL6 profile indicates missing values during mock infection. A fold-change of 1 indicates no change from mock. See also Figure S3.

(G) Temporal profiles of selected cellular proteins classified as positive innate immunity regulators. Fold-change values were calculated as in F. See also Figure S3.

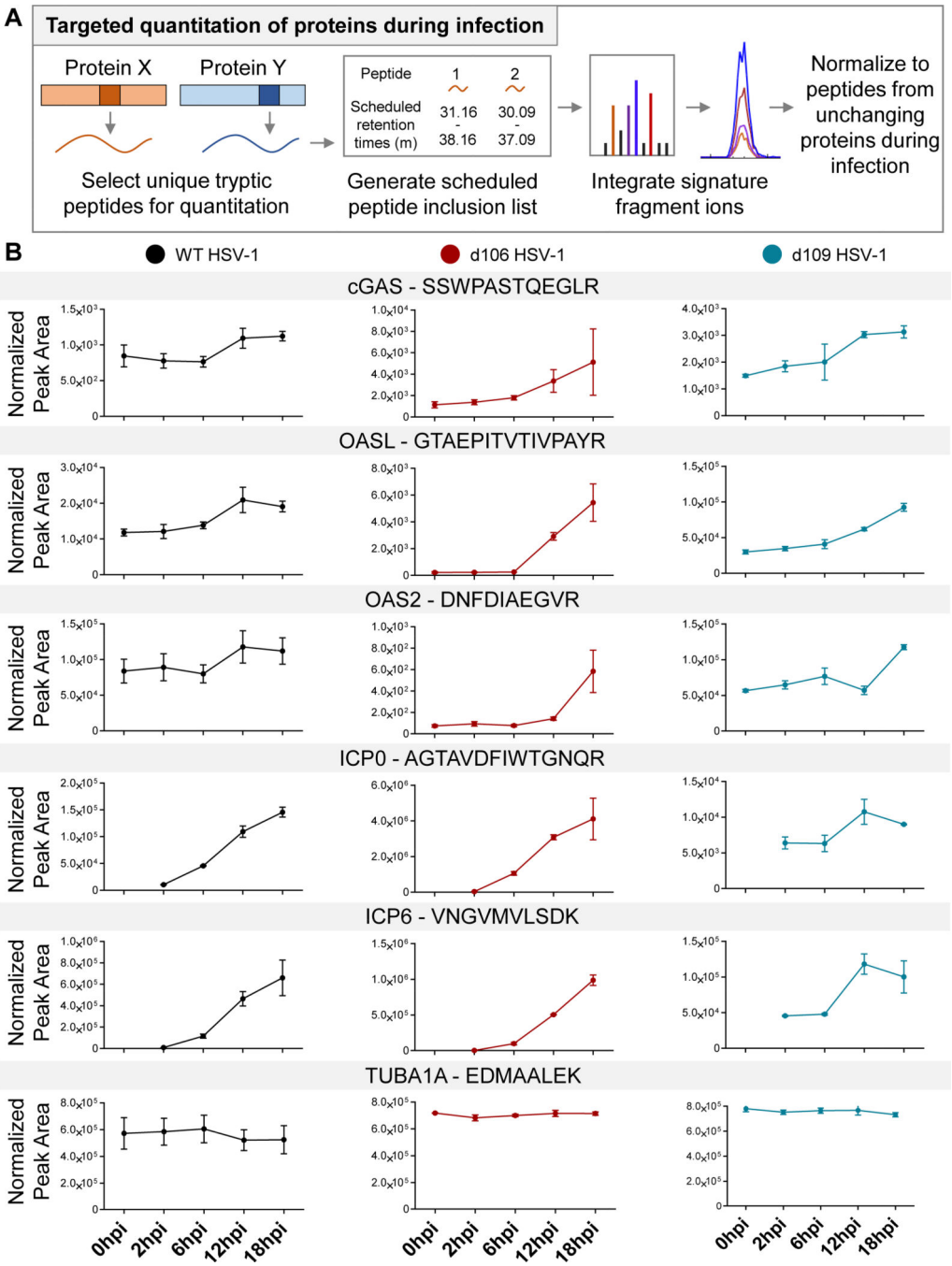

Fig. 4. Endogenous cGAS, OASL and OAS2 protein abundances increase during *d106* and *d109* HSV-1 infections, compared to WT HSV-1 infection.

(A) Workflow for targeted PRM analysis of endogenous cGAS, OASL, and OAS2 in HFFs throughout the HSV-1 replication cycle.

(B) Peak areas of representative peptides for cGAS, OASL, and OAS2, normalized to global standards (TUBA1A, MYH9) during WT, *d106*, and *d109* infections.

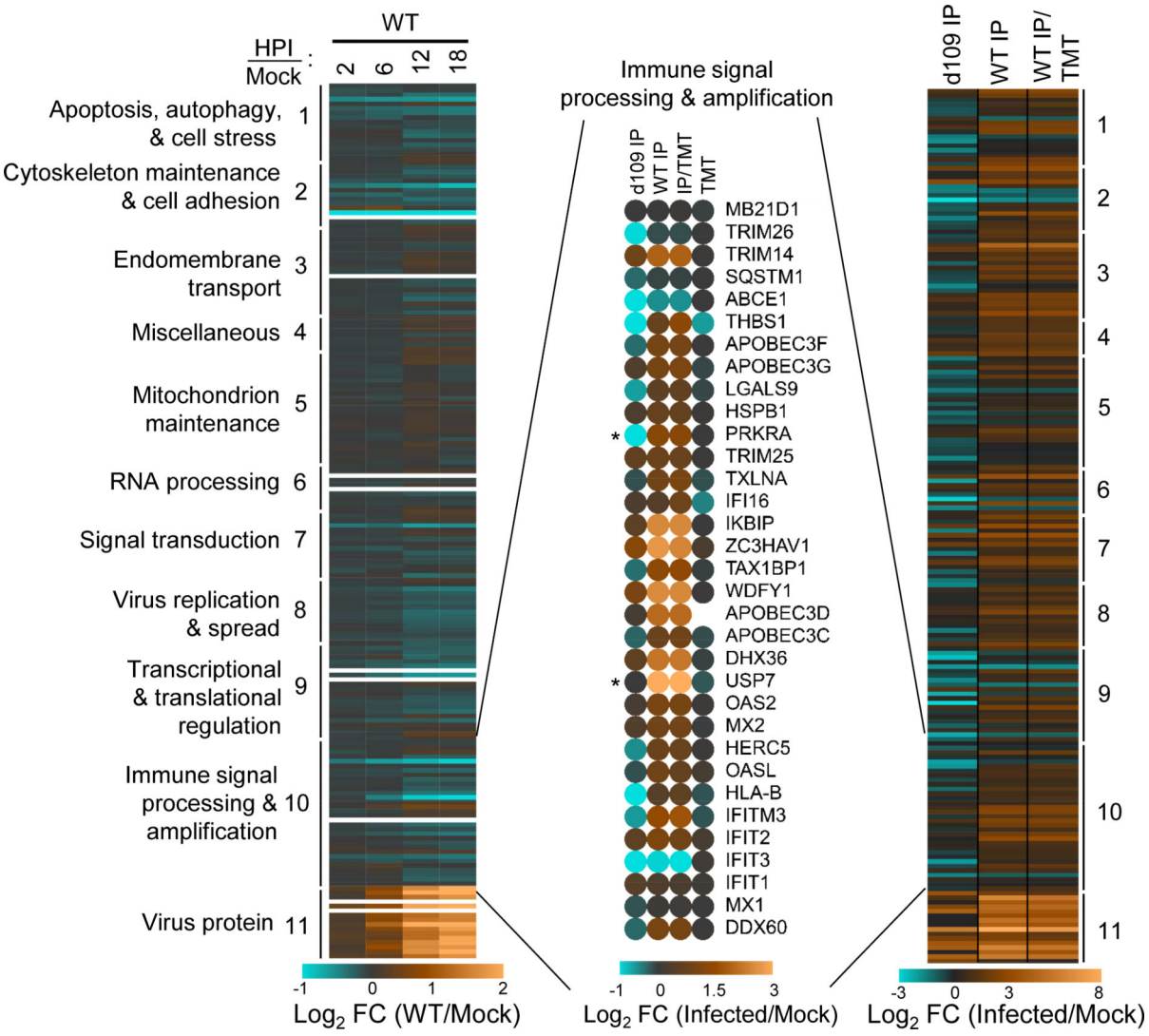

Fig. 5. cGAS protein interactions are not primarily driven by alterations in protein abundances.

Temporal protein abundance alterations for the identified cGAS interactions (left; numbers and classifications match Fig. 2 clusters). Interaction levels were normalized to their respective protein abundances (right, WT IP/TMT). Consistency of cGAS interactions during *d109* infection was determined (right, *d109* IP). Inset shows abundances and IP enrichment values for the immune signaling category of cGAS interactions. Asterisks indicate absence of interaction with GFP-cGAS during *d109* infection.

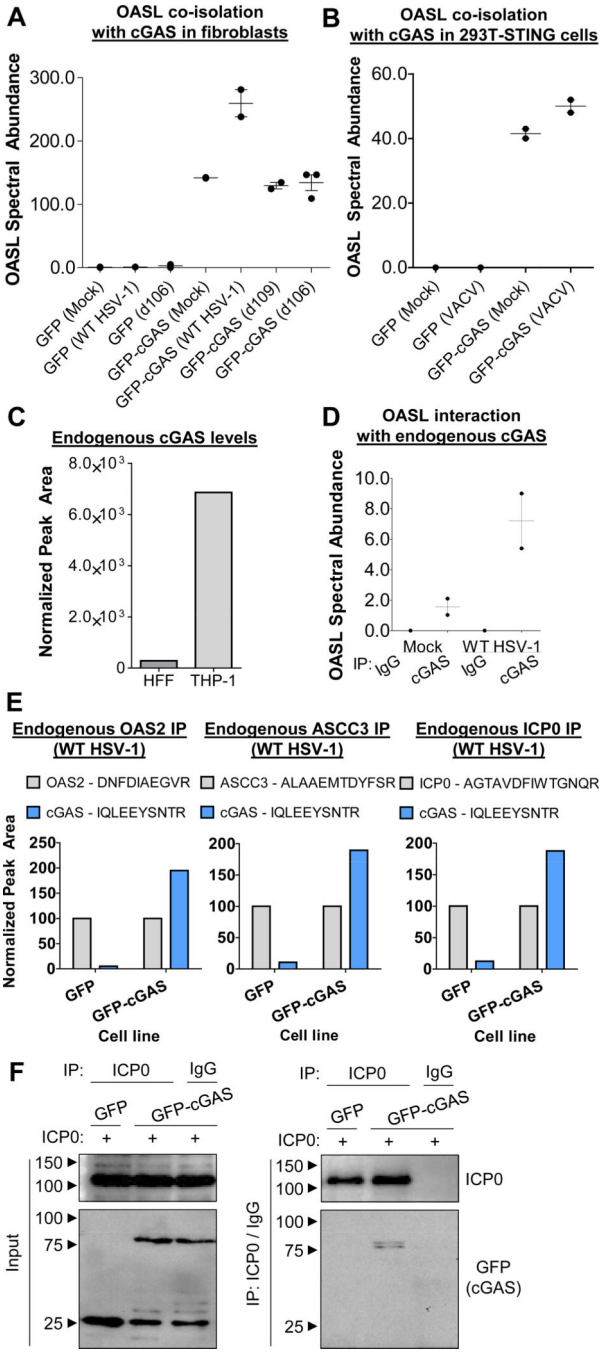

Fig. 6. The cGAS-OASL interaction is maintained in multiple cell types.

(A, B) Spectral abundances of OASL quantified after IP-MS of GFP-cGAS in (A) HFFs during mock, WT, *d106*, and *d109* infections (MOI 5, 6 hpi), and (B) HEK293T-STINGs during mock and VACV 70mer transfections (6 h post-transfection). IPs were normalized to cGAS bait. See also Figure S4.

(C) Peak areas from PRM of a representative peptide (SSWPASTQEGLR) for endogenous cGAS levels, normalized to TUBA1A in HFFs and differentiated THP-1 monocytes.

(D) Identification of OASL interaction with endogenous cGAS in differentiated THP-1 monocytes (mock or WT HSV-1 infected). IgG control isolations were conducted in parallel. (E) Validation of cGAS interactions via reciprocal co-IP of endogenous proteins (OAS2, ASCC3, viral ICP0) and PRM. GFP and GFP-cGAS HFFs were infected with WT HSV-1 (MOI 5, 6 hpi). PRM peak areas of representative peptides for each protein are shown. (F) Validation of the cGAS-ICP0 interaction by reciprocal co-IP and Western blot. HEK293Ts were co-transfected with ICP0 and either GFP, or GFP-cGAS.

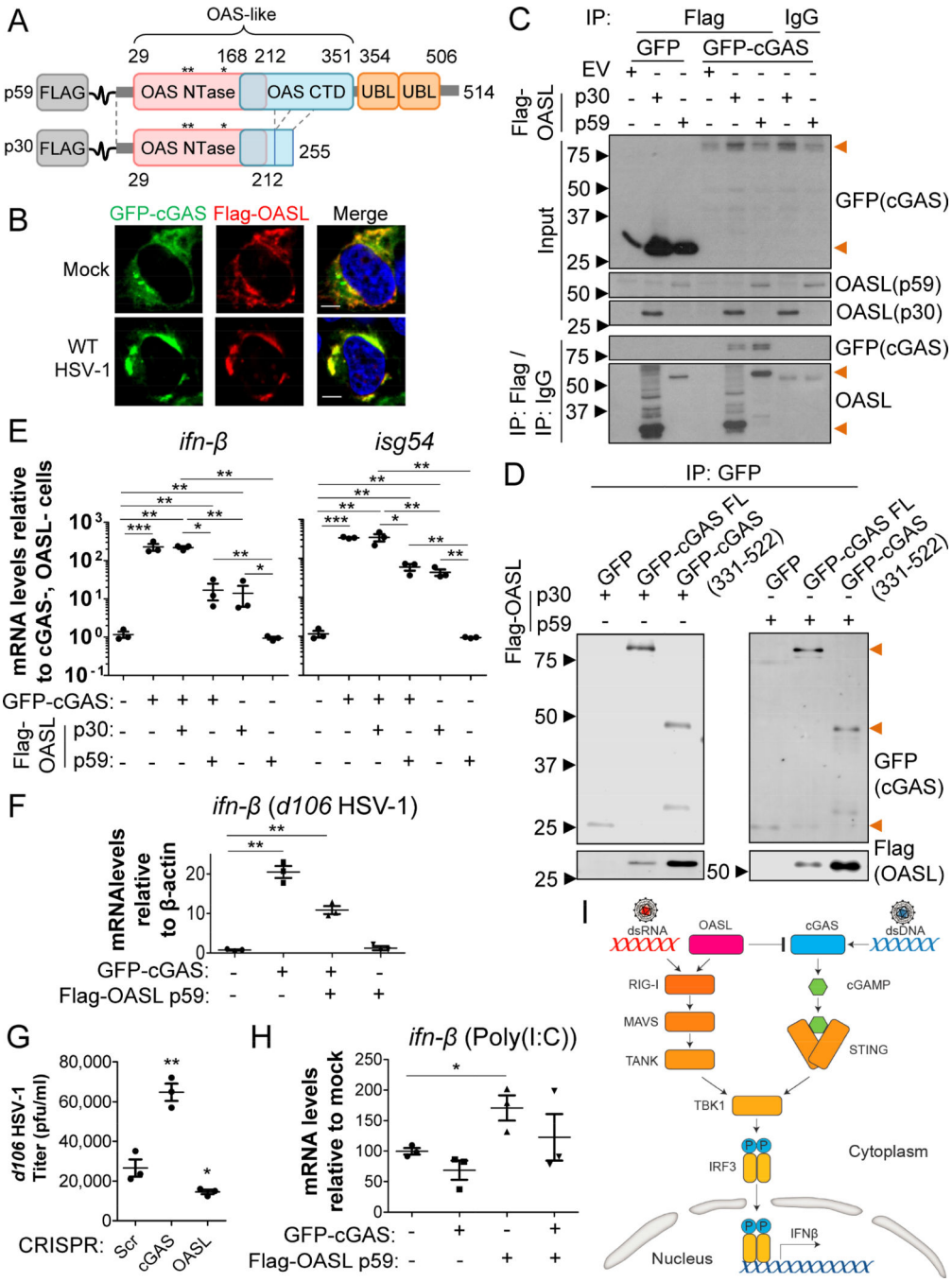

Fig. 7. The oligoadenylate synthase-like domain of OASL binds to the Mab21 domain of cGAS and inhibits cGAS-dependent Type I IFN induction.

(A) Schematic of Flag-OASL p30 and p59 constructs. Asterisks denote residue differences between OAS1/2/3 and OASL in the NTase domain catalytic triad.

(B) Immunofluorescence microscopy of GFP-cGAS and FLAG-OASL p59 in transfected HFFs either uninfected, or infected with WT HSV-1 (MOI 5, 6 hpi). Size bars, 5 μm.

(C) Validation and isoform assessment of the cGAS-OASL interaction by reciprocal co-IP and Western blot. HEK293Ts were co-transfected with GFP-cGAS and Flag-OASL (p30 or p59) and doxycycline-induced. Flag-OASL was isolated via anti-Flag antibody, and IgG was

used for control IPs. Bands in IgG IP lanes (bottom blot) at 50 kDa are antibody heavy chain.

(D) cGAS domain assessment of the cGAS-OASL interaction by co-IP and Western blot. Cells were co-transfected with Flag-OASL and GFP-cGAS domains as in (A), and cGAS was isolated via anti-GFP antibody.

(E) STING, GFP-cGAS, and Flag-OASL (p30 or p59) constructs were co-transfected into HEK293Ts and doxycycline-induced. *ifn-β* and *isg54* mRNA levels were assessed by qRT-PCR. $n = 3$. Error bars= S.E.M. Significantly different values ($P \leq 0.01$) are indicated by Student's t test: *, $P \leq 0.05$; **, $P \leq 0.01$; ***, $P \leq 0.001$.

(F) STING, GFP-cGAS, and Flag-OASL p59 constructs were co-transfected into HEK293Ts and doxycycline-induced. Cells were infected with WT HSV-1 (MOI 5, 6 hpi). *ifn-β* mRNA levels were assessed by qRT-PCR. $n = 3$. Error bars= S.E.M. Significantly different values ($P \leq 0.01$) from that of control cells are indicated by Student's t (**).

(G) Virus progeny titers on E11 cells of CRISPR HFFs (sgScrambled, sgcGAS, and sgOASL) infected with *d106* HSV-1 (MOI 0.2). Significantly different values from that of CRISPR-Scrambled are indicated by Student's t test: *, $P \leq 0.05$; **, $P \leq 0.01$. See also Figure S5.

(H) GFP-cGAS and Flag-OASL p59 constructs were co-transfected with poly (I:C) (1 μg/ml) into HEK293Ts and doxycycline-induced. *ifn-β* mRNA levels were assessed by qRT-PCR. $n = 3$. Error bars= S.E.M. Significantly different values ($P \leq 0.05$) from that of control cells are indicated by Student's t (*).

(I) Model for the proposed homeostatic regulation of cGAS by OASL in a resting cell state and during active immune signaling.